Measurement of the inclusive jet cross section using the k_T algorithm in $p\bar{p}$ collisions at $\sqrt{s} = 1.96$ TeV with the CDF II detector

A. Abulencia,[24] J. Adelman,[13] T. Affolder,[10] T. Akimoto,[56] M. G. Albrow,[17] D. Ambrose,[17] S. Amerio,[44] D. Amidei,[35] A. Anastassov,[53] K. Anikeev,[17] A. Annovi,[19] J. Antos,[14] M. Aoki,[56] G. Apollinari,[17] J.-F. Arguin,[34] T. Arisawa,[58] A. Artikov,[15] W. Ashmanskas,[17] A. Attal,[8] F. Azfar,[43] P. Azzi-Bacchetta,[44] P. Azzurri,[47] N. Bacchetta,[44] W. Badgett,[17] A. Barbaro-Galtieri,[29] V. E. Barnes,[49] B. A. Barnett,[25] S. Baroiant,[7] V. Bartsch,[31] G. Bauer,[33] F. Bedeschi,[47] S. Behari,[25] S. Belforte,[55] G. Bellettini,[47] J. Bellinger,[60] A. Belloni,[33] D. Benjamin,[16] A. Beretvas,[17] J. Beringer,[29] T. Berry,[30] A. Bhatti,[51] M. Binkley,[17] D. Bisello,[44] R. E. Blair,[2] C. Blocker,[6] B. Blumenfeld,[25] A. Bocci,[16] A. Bodek,[50] V. Boisvert,[50] G. Bolla,[49] A. Bolshov,[33] D. Bortoletto,[49] J. Boudreau,[48] A. Boveia,[10] B. Brau,[10] L. Brigliadori,[5] C. Bromberg,[36] E. Brubaker,[13] J. Budagov,[15] H. S. Budd,[50] S. Budd,[24] S. Budroni,[47] K. Burkett,[17] G. Busetto,[44] P. Bussey,[21] K. L. Byrum,[2] S. Cabrera,[16,o] M. Campanelli,[20] M. Campbell,[35] F. Canelli,[17] A. Canepa,[49] S. Carillo,[18,i] D. Carlsmith,[60] R. Carosi,[47] S. Carron,[34] M. Casarsa,[55] A. Castro,[5] P. Catastini,[47] D. Cauz,[55] M. Cavalli-Sforza,[3] A. Cerri,[29] L. Cerrito,[43,m] S. H. Chang,[28] Y. C. Chen,[1] M. Chertok,[7] G. Chiarelli,[47] G. Chlachidze,[15] F. Chlebana,[17] I. Cho,[28] K. Cho,[28] D. Chokheli,[15] J. P. Chou,[22] G. Choudalakis,[33] S. H. Chuang,[60] K. Chung,[12] W. H. Chung,[60] Y. S. Chung,[50] M. Ciljak,[47] C. I. Ciobanu,[24] M. A. Ciocci,[47] A. Clark,[20] D. Clark,[6] M. Coca,[16] G. Compostella,[44] M. E. Convery,[51] J. Conway,[7] B. Cooper,[36] K. Copic,[35] M. Cordelli,[19] G. Cortiana,[44] F. Crescioli,[47] C. Cuenca Almenar,[7,o] J. Cuevas,[11,l] R. Culbertson,[17] J. C. Cully,[35] D. Cyr,[60] S. DaRonco,[44] M. Datta,[17] S. D'Auria,[21] T. Davies,[21] M. D'Onofrio,[3] D. Dagenhart,[6] P. de Barbaro,[50] S. De Cecco,[52] A. Deisher,[29] G. De Lentdecker,[50,c] M. Dell'Orso,[47] F. Delli Paoli,[44] L. Demortier,[51] J. Deng,[16] M. Deninno,[5] D. De Pedis,[52] P. F. Derwent,[17] G. P. Di Giovanni,[45] C. Dionisi,[52] B. Di Ruzza,[55] J. R. Dittmann,[4] P. DiTuro,[53] C. Dörr,[26] S. Donati,[47] M. Donega,[20] P. Dong,[8] J. Donini,[44] T. Dorigo,[44] S. Dube,[53] J. Efron,[40] R. Erbacher,[7] D. Errede,[24] S. Errede,[24] R. Eusebi,[17] H. C. Fang,[29] S. Farrington,[30] I. Fedorko,[47] W. T. Fedorko,[13] R. G. Feild,[61] M. Feindt,[26] J. P. Fernandez,[32] R. Field,[18] G. Flanagan,[49] A. Foland,[22] S. Forrester,[7] G. W. Foster,[17] M. Franklin,[22] J. C. Freeman,[29] I. Furic,[13] M. Gallinaro,[51] J. Galyardt,[12] J. E. Garcia,[47] F. Garberson,[10] A. F. Garfinkel,[49] C. Gay,[61] H. Gerberich,[24] D. Gerdes,[35] S. Giagu,[52] P. Giannetti,[47] A. Gibson,[29] K. Gibson,[48] J. L. Gimmell,[50] C. Ginsburg,[17] N. Giokaris,[15,a] M. Giordani,[55] P. Giromini,[19] M. Giunta,[47] G. Giurgiu,[12] V. Glagolev,[15] D. Glenzinski,[17] M. Gold,[38] N. Goldschmidt,[18] J. Goldstein,[43,b] A. Golossanov,[17] G. Gomez,[11] G. Gomez-Ceballos,[11] M. Goncharov,[54] O. González,[32] I. Gorelov,[38] A. T. Goshaw,[16] K. Goulianos,[51] A. Gresele,[44] M. Griffiths,[30] S. Grinstein,[22] C. Grosso-Pilcher,[13] R. C. Group,[18] U. Grundler,[24] J. Guimaraes da Costa,[22] Z. Gunay-Unalan,[36] C. Haber,[29] K. Hahn,[33] S. R. Hahn,[17] E. Halkiadakis,[53] A. Hamilton,[34] B.-Y. Han,[50] J. Y. Han,[50] R. Handler,[60] F. Happacher,[19] K. Hara,[56] M. Hare,[57] S. Harper,[43] R. F. Harr,[59] R. M. Harris,[17] M. Hartz,[48] K. Hatakeyama,[51] J. Hauser,[8] A. Heijboer,[46] B. Heinemann,[30] J. Heinrich,[46] C. Henderson,[33] M. Herndon,[60] J. Heuser,[26] D. Hidas,[16] C. S. Hill,[10,b] D. Hirschbuehl,[26] A. Hocker,[17] A. Holloway,[22] S. Hou,[1] M. Houlden,[30] S.-C. Hsu,[9] B. T. Huffman,[43] R. E. Hughes,[40] U. Husemann,[61] J. Huston,[36] J. Incandela,[10] G. Introzzi,[47] M. Iori,[52] Y. Ishizawa,[56] A. Ivanov,[7] B. Iyutin,[33] E. James,[17] D. Jang,[53] B. Jayatilaka,[35] D. Jeans,[52] H. Jensen,[17] E. J. Jeon,[28] S. Jindariani,[18] M. Jones,[49] K. K. Joo,[28] S. Y. Jun,[12] J. E. Jung,[28] T. R. Junk,[24] T. Kamon,[54] P. E. Karchin,[59] Y. Kato,[42] Y. Kemp,[26] R. Kephart,[17] U. Kerzel,[26] V. Khotilovich,[54] B. Kilminster,[40] D. H. Kim,[28] H. S. Kim,[28] J. E. Kim,[28] M. J. Kim,[12] S. B. Kim,[28] S. H. Kim,[56] Y. K. Kim,[13] N. Kimura,[56] L. Kirsch,[6] S. Klimenko,[18] M. Klute,[33] B. Knuteson,[33] B. R. Ko,[16] K. Kondo,[58] D. J. Kong,[28] J. Konigsberg,[18] A. Korytov,[18] A. V. Kotwal,[16] A. Kovalev,[46] A. C. Kraan,[46] J. Kraus,[24] I. Kravchenko,[33] M. Kreps,[26] J. Kroll,[46] N. Krumnack,[4] M. Kruse,[16] V. Krutelyov,[10] T. Kubo,[56] S. E. Kuhlmann,[2] T. Kuhr,[26] Y. Kusakabe,[58] S. Kwang,[13] A. T. Laasanen,[49] S. Lai,[34] S. Lami,[47] S. Lammel,[17] M. Lancaster,[31] R. L. Lander,[7] K. Lannon,[40] A. Lath,[53] G. Latino,[47] I. Lazzizzera,[44] T. LeCompte,[2] J. Lee,[50] J. Lee,[28] Y. J. Lee,[28] S. W. Lee,[54,n] R. Lefèvre,[3] N. Leonardo,[33] S. Leone,[47] S. Levy,[13] J. D. Lewis,[17] C. Lin,[61] C. S. Lin,[17] M. Lindgren,[17] E. Lipeles,[9] A. Lister,[7] D. O. Litvintsev,[17] T. Liu,[17] N. S. Lockyer,[46] A. Loginov,[61] M. Loreti,[44] P. Loverre,[52] R.-S. Lu,[1] D. Lucchesi,[44] P. Lujan,[29] P. Lukens,[17] G. Lungu,[18] L. Lyons,[43] J. Lys,[29] R. Lysak,[14] E. Lytken,[49] P. Mack,[26] D. MacQueen,[34] R. Madrak,[17] K. Maeshima,[17] K. Makhoul,[33] T. Maki,[23] P. Maksimovic,[25] S. Malde,[43] G. Manca,[30] F. Margaroli,[5] R. Marginean,[17] C. Marino,[26] C. P. Marino,[24] A. Martin,[61] M. Martin,[25] V. Martin,[21,g] M. Martínez,[3] T. Maruyama,[56] P. Mastrandrea,[52] T. Masubuchi,[56] H. Matsunaga,[56] M. E. Mattson,[59] R. Mazini,[34] P. Mazzanti,[5] K. S. McFarland,[50] P. McIntyre,[54] R. McNulty,[30,f] A. Mehta,[30] P. Mehtala,[23] S. Menzemer,[11,h] A. Menzione,[47] P. Merkel,[49] C. Mesropian,[51] A. Messina,[36] T. Miao,[17] N. Miladinovic,[6] J. Miles,[33] R. Miller,[36] C. Mills,[10] M. Milnik,[26] A. Mitra,[1] G. Mitselmakher,[18] A. Miyamoto,[27] S. Moed,[20] N. Moggi,[5] B. Mohr,[8] R. Moore,[17] M. Morello,[47] P. Movilla Fernandez,[29] J. Mülmenstädt,[29] A. Mukherjee,[17] Th. Muller,[26] R. Mumford,[25] P. Murat,[17] J. Nachtman,[17]

A. Nagano,[56] J. Naganoma,[58] I. Nakano,[41] A. Napier,[57] V. Necula,[18] C. Neu,[46] M. S. Neubauer,[9] J. Nielsen,[29] T. Nigmanov,[48] L. Nodulman,[2] O. Norniella,[3] E. Nurse,[31] S. H. Oh,[16] Y. D. Oh,[28] I. Oksuzian,[18] T. Okusawa,[42] R. Oldeman,[30] R. Orava,[23] K. Osterberg,[23] C. Pagliarone,[47] E. Palencia,[11] V. Papadimitriou,[17] A. A. Paramonov,[13] B. Parks,[40] S. Pashapour,[34] J. Patrick,[17] G. Pauletta,[55] M. Paulini,[12] C. Paus,[33] D. E. Pellett,[7] A. Penzo,[55] T. J. Phillips,[16] G. Piacentino,[47] J. Piedra,[45] L. Pinera,[18] K. Pitts,[24] C. Plager,[8] L. Pondrom,[60] X. Portell,[3] O. Poukhov,[15] N. Pounder,[43] F. Prakoshyn,[15] A. Pronko,[17] J. Proudfoot,[2] F. Ptohos,[19,e] G. Punzi,[47] J. Pursley,[25] J. Rademacker,[43,b] A. Rahaman,[48] N. Ranjan,[49] S. Rappoccio,[22] B. Reisert,[17] V. Rekovic,[38] P. Renton,[43] M. Rescigno,[52] S. Richter,[26] F. Rimondi,[5] L. Ristori,[47] A. Robson,[21] T. Rodrigo,[11] E. Rogers,[24] S. Rolli,[57] R. Roser,[17] M. Rossi,[55] R. Rossin,[18] A. Ruiz,[11] J. Russ,[12] V. Rusu,[13] H. Saarikko,[23] S. Sabik,[34] A. Safonov,[54] W. K. Sakumoto,[50] G. Salamanna,[52] O. Saltó,[3] D. Saltzberg,[8] C. Sánchez,[3] L. Santi,[55] S. Sarkar,[52] L. Sartori,[47] K. Sato,[17] P. Savard,[34] A. Savoy-Navarro,[45] T. Scheidle,[26] P. Schlabach,[17] E. E. Schmidt,[17] M. P. Schmidt,[61] M. Schmitt,[39] T. Schwarz,[7] L. Scodellaro,[11] A. L. Scott,[10] A. Scribano,[47] F. Scuri,[47] A. Sedov,[49] S. Seidel,[38] Y. Seiya,[42] A. Semenov,[15] L. Sexton-Kennedy,[17] A. Sfyrla,[20] M. D. Shapiro,[29] T. Shears,[30] P. F. Shepard,[48] D. Sherman,[22] M. Shimojima,[56,k] M. Shochet,[13] Y. Shon,[60] I. Shreyber,[37] A. Sidoti,[47] P. Sinervo,[34] A. Sisakyan,[15] J. Sjolin,[43] A. J. Slaughter,[17] J. Slaunwhite,[40] K. Sliwa,[57] J. R. Smith,[7] F. D. Snider,[17] R. Snihur,[34] M. Soderberg,[35] A. Soha,[7] S. Somalwar,[53] V. Sorin,[36] J. Spalding,[17] F. Spinella,[47] T. Spreitzer,[34] P. Squillacioti,[47] M. Stanitzki,[61] A. Staveris-Polykalas,[47] R. St. Denis,[21] B. Stelzer,[8] O. Stelzer-Chilton,[43] D. Stentz,[39] J. Strologas,[38] D. Stuart,[10] J. S. Suh,[28] A. Sukhanov,[18] H. Sun,[57] T. Suzuki,[56] A. Taffard,[24] R. Takashima,[41] Y. Takeuchi,[56] K. Takikawa,[56] M. Tanaka,[2] R. Tanaka,[41] M. Tecchio,[35] P. K. Teng,[1] K. Terashi,[51] J. Thom,[17,d] A. S. Thompson,[21] E. Thomson,[46] P. Tipton,[61] V. Tiwari,[12] S. Tkaczyk,[17] D. Toback,[54] S. Tokar,[14] K. Tollefson,[36] T. Tomura,[56] D. Tonelli,[47] S. Torre,[19] D. Torretta,[17] S. Tourneur,[45] W. Trischuk,[34] R. Tsuchiya,[58] S. Tsuno,[41] N. Turini,[47] F. Ukegawa,[56] T. Unverhau,[21] S. Uozumi,[56] D. Usynin,[46] S. Vallecorsa,[20] N. van Remortel,[23] A. Varganov,[35] E. Vataga,[38] F. Vázquez,[18,i] G. Velev,[17] G. Veramendi,[24] V. Veszpremi,[49] R. Vidal,[17] I. Vila,[11] R. Vilar,[11] T. Vine,[31] I. Vollrath,[34] I. Volobouev,[29,n] G. Volpi,[47] F. Würthwein,[9] P. Wagner,[54] R. G. Wagner,[2] R. L. Wagner,[17] J. Wagner,[26] W. Wagner,[26] R. Wallny,[8] S. M. Wang,[1] A. Warburton,[34] S. Waschke,[21] D. Waters,[31] M. Weinberger,[54] W. C. Wester III,[17] B. Whitehouse,[57] D. Whiteson,[46] A. B. Wicklund,[2] E. Wicklund,[17] G. Williams,[34] H. H. Williams,[46] P. Wilson,[17] B. L. Winer,[40] P. Wittich,[17,d] S. Wolbers,[17] C. Wolfe,[13] T. Wright,[35] X. Wu,[20] S. M. Wynne,[30] A. Yagil,[17] K. Yamamoto,[42] J. Yamaoka,[53] T. Yamashita,[41] C. Yang,[61] U. K. Yang,[13,j] Y. C. Yang,[28] W. M. Yao,[29] G. P. Yeh,[17] J. Yoh,[17] K. Yorita,[13] T. Yoshida,[42] G. B. Yu,[50] I. Yu,[28] S. S. Yu,[17] J. C. Yun,[17] L. Zanello,[52] A. Zanetti,[55] I. Zaw,[22] X. Zhang,[24] J. Zhou,[53] and S. Zucchelli[5]

(CDF Collaboration)

[1]*Institute of Physics, Academia Sinica, Taipei, Taiwan 11529, Republic of China*
[2]*Argonne National Laboratory, Argonne, Illinois 60439, USA*
[3]*Institut de Fisica d'Altes Energies, Universitat Autonoma de Barcelona, E-08193, Bellaterra (Barcelona), Spain*
[4]*Baylor University, Waco, Texas 76798, USA*
[5]*Istituto Nazionale di Fisica Nucleare, University of Bologna, I-40127 Bologna, Italy*
[6]*Brandeis University, Waltham, Massachusetts 02254, USA*
[7]*University of California, Davis, Davis, California 95616, USA*
[8]*University of California, Los Angeles, Los Angeles, California 90024, USA*
[9]*University of California, San Diego, La Jolla, California 92093, USA*
[10]*University of California, Santa Barbara, Santa Barbara, California 93106, USA*
[11]*Instituto de Fisica de Cantabria, CSIC-University of Cantabria, 39005 Santander, Spain*
[12]*Carnegie Mellon University, Pittsburgh, Pennsylvania 15213, USA*
[13]*Enrico Fermi Institute, University of Chicago, Chicago, Illinois 60637, USA*
[14]*Comenius University, 842 48 Bratislava, Slovakia; Institute of Experimental Physics, 040 01 Kosice, Slovakia*
[15]*Joint Institute for Nuclear Research, RU-141980 Dubna, Russia*
[16]*Duke University, Durham, North Carolina 27708, USA*
[17]*Fermi National Accelerator Laboratory, Batavia, Illinois 60510, USA*
[18]*University of Florida, Gainesville, Florida 32611, USA*
[19]*Laboratori Nazionali di Frascati, Istituto Nazionale di Fisica Nucleare, I-00044 Frascati, Italy*
[20]*University of Geneva, CH-1211 Geneva 4, Switzerland*
[21]*Glasgow University, Glasgow G12 8QQ, United Kingdom*
[22]*Harvard University, Cambridge, Massachusetts 02138, USA*
[23]*Division of High Energy Physics, Department of Physics, University of Helsinki, and Helsinki Institute of Physics, FIN-00014, Helsinki, Finland*

[24]University of Illinois, Urbana, Illinois 61801, USA
[25]The Johns Hopkins University, Baltimore, Maryland 21218, USA
[26]Institut für Experimentelle Kernphysik, Universität Karlsruhe, 76128 Karlsruhe, Germany
[27]High Energy Accelerator Research Organization (KEK), Tsukuba, Ibaraki 305, Japan
[28]Center for High Energy Physics: Kyungpook National University, Taegu 702-701, Korea; Seoul National University, Seoul 151-742, Korea; and SungKyunKwan University, Suwon 440-746, Korea
[29]Ernest Orlando Lawrence Berkeley National Laboratory, Berkeley, California 94720, USA
[30]University of Liverpool, Liverpool L69 7ZE, United Kingdom
[31]University College London, London WC1E 6BT, United Kingdom
[32]Centro de Investigaciones Energeticas Medioambientales y Tecnologicas, E-28040 Madrid, Spain
[33]Massachusetts Institute of Technology, Cambridge, Massachusetts 02139, USA
[34]Institute of Particle Physics: McGill University, Montréal, Canada H3A 2T8; and University of Toronto, Toronto, Canada M5S 1A7
[35]University of Michigan, Ann Arbor, Michigan 48109, USA
[36]Michigan State University, East Lansing, Michigan 48824, USA
[37]Institution for Theoretical and Experimental Physics, ITEP, Moscow 117259, Russia
[38]University of New Mexico, Albuquerque, New Mexico 87131, USA
[39]Northwestern University, Evanston, Illinois 60208, USA
[40]The Ohio State University, Columbus, Ohio 43210, USA
[41]Okayama University, Okayama 700-8530, Japan
[42]Osaka City University, Osaka 588, Japan
[43]University of Oxford, Oxford OX1 3RH, United Kingdom
[44]University of Padova, Istituto Nazionale di Fisica Nucleare, Sezione di Padova-Trento, I-35131 Padova, Italy
[45]LPNHE, Universite Pierre et Marie Curie/IN2P3-CNRS, UMR7585, Paris, F-75252 France
[46]University of Pennsylvania, Philadelphia, Pennsylvania 19104, USA
[47]Istituto Nazionale di Fisica Nucleare Pisa, Universities of Pisa, Siena and Scuola Normale Superiore, I-56127 Pisa, Italy
[48]University of Pittsburgh, Pittsburgh, Pennsylvania 15260, USA
[49]Purdue University, West Lafayette, Indiana 47907, USA
[50]University of Rochester, Rochester, New York 14627, USA
[51]The Rockefeller University, New York, New York 10021, USA
[52]Istituto Nazionale di Fisica Nucleare, Sezione di Roma 1, University of Rome "La Sapienza", I-00185 Roma, Italy
[53]Rutgers University, Piscataway, New Jersey 08855, USA
[54]Texas A&M University, College Station, Texas 77843, USA
[55]Istituto Nazionale di Fisica Nucleare, University of Trieste/Udine, Italy
[56]University of Tsukuba, Tsukuba, Ibaraki 305, Japan
[57]Tufts University, Medford, Massachusetts 02155, USA
[58]Waseda University, Tokyo 169, Japan
[59]Wayne State University, Detroit, Michigan 48201, USA
[60]University of Wisconsin, Madison, Wisconsin 53706, USA
[61]Yale University, New Haven, Connecticut 06520, USA

(Received 29 January 2007; published 24 May 2007; publisher error corrected 25 May 2007)

We report on measurements of the inclusive jet production cross section as a function of the jet transverse momentum in $p\bar{p}$ collisions at $\sqrt{s} = 1.96$ TeV, using the k_T algorithm and a data sample corresponding to 1.0 fb^{-1} collected with the Collider Detector at Fermilab in run II. The measurements are carried out in five different jet rapidity regions with $|y^{\text{jet}}| < 2.1$ and transverse momentum in the range

[a]Visiting scientist from University of Athens, 157 84 Athens, Greece.
[b]Visiting scientist from University of Bristol, Bristol BS8 1TL, United Kingdom.
[c]Visiting scientist from Universite Libre de Bruxelles (ULB), B-1050 Brussels, Belgium.
[d]Visiting scientist from Cornell University, Ithaca, NY 14853, USA.
[e]Visiting scientist from University of Cyprus, Nicosia CY-1678, Cyprus.
[f]Visiting scientist from University College Dublin, Dublin 4, Ireland.
[g]Visiting scientist from University of Edinburgh, Edinburgh EH9 3JZ, United Kingdom.
[h]Visiting scientist from University of Heidelberg, D-69120 Heidelberg, Germany.
[i]Visiting scientist from University of Iberoamericana, Mexico D.F., Mexico.
[j]Visiting scientist from University of Manchester, Manchester M13 9PL, United Kingdom.
[k]Visiting scientist from Nagasaki Institute of Applied Science, Nagasaki, Japan.
[l]Visiting scientist from Universidad de Oviedo, E-33007 Oviedo, Spain.
[m]Visiting scientist from Queen Mary and Westfield College, London, E1 4NS, United Kingdom.
[n]Visiting scientist from Texas Tech University, Lubbock, TX 79409, USA.
[o]Visiting scientist from Instituto de Fisica Corpuscular (IFIC), 46071 Valencia, Spain.

$54 < p_T^{jet} < 700$ GeV/c. Next-to-leading order perturbative QCD predictions are in good agreement with the measured cross sections.

DOI: 10.1103/PhysRevD.75.092006 PACS numbers: 12.38.Aw, 13.85.−t, 13.87.−a

I. INTRODUCTION

The measurement of the inclusive jet cross section as a function of the jet transverse momentum, p_T^{jet}, in $p\bar{p}$ collisions at $\sqrt{s} = 1.96$ TeV constitutes a test of perturbative quantum chromodynamics (pQCD) [1]. In run II [2] of the Tevatron, measurements of the jet cross section for jets with p_T^{jet} up to about 700 GeV/c [3,4] have extended the p_T^{jet} range by more than 150 GeV/c compared to run I [5–7]. In particular, the CDF collaboration recently published results [3] on inclusive jet production using the k_T algorithm [8,9] for jets with $p_T^{jet} > 54$ GeV/c and rapidity [10] in the region $0.1 < |y^{jet}| < 0.7$, which are well described by next-to-leading order (NLO) pQCD predictions [11]. As discussed in [3], the k_T algorithm has been widely used for precise QCD measurements at both e^+e^- and $e^{\pm}p$ colliders, and makes possible a well-defined comparison to the theoretical predictions [9]. The pQCD calculations involve matrix elements, describing the hard interaction between partons, convoluted with parton density functions (PDFs) [12,13] in the proton and antiproton that require input from experiment. The pQCD predictions are affected by the still-limited knowledge of the gluon PDF, which translates into a large uncertainty on the theoretical cross sections at high p_T^{jet} [3,4]. Inclusive jet cross section measurements from run I at the Tevatron [6], performed in different jet rapidity regions, have been used to partially constrain the gluon distribution in the proton. This article continues the studies on jet production using the k_T algorithm at the Tevatron [3,7] and presents new measurements of the inclusive jet production cross section as a function of p_T^{jet} in five different jet rapidity regions up to $|y^{jet}| = 2.1$, based on 1.0 fb^{-1} of CDF run II data. The measurements are corrected to the hadron level [14] and compared to NLO pQCD predictions.

II. EXPERIMENTAL SETUP

The CDF II detector (see Fig. 1) is described in detail in [15]. The subdetectors most relevant for this analysis are discussed briefly here. The detector has a charged particle tracking system immersed in a 1.4 T magnetic field. A silicon microstrip detector [16] provides tracking over the radial range 1.35 to 28 cm and covers the pseudorapidity range $|\eta| < 2$. A 3.1-m-long open-cell drift chamber [17] covers the radial range from 44 to 132 cm and provides tracking coverage for $|\eta| < 1$. Segmented sampling calorimeters, arranged in a projective tower geometry, surround the tracking system and measure the energy of interacting particles for $|\eta| < 3.6$. The central barrel calorimeter [18] covers the region $|\eta| < 1$. It consists of two sections, an electromagnetic calorimeter (CEM) and a hadronic calorimeter (CHA), divided into 480 towers of size 0.1 in η and 0.26 in ϕ. The end-wall hadronic calorimeter (WHA) [19] is behind the central barrel calorimeter in the region $0.6 < |\eta| < 1.0$, providing forward coverage out to $|\eta| < 1.3$. In run II, new forward scintillator-plate calorimeters [20] replaced the run I gas calorimeter system. The new plug electromagnetic calorimeter (PEM) covers the region $1.1 < |\eta| < 3.6$, while the new hadronic calorimeter (PHA) provides coverage in the $1.3 < |\eta| < 3.6$ region. The calorimeter has gaps at $|\eta| \approx 0$ (between the two halves of the central barrel calorimeter) and at $|\eta| \approx 1.1$ (in the region between the WHA and the plug calorimeters). The measured energy resolutions for electrons in the electromagnetic calorimeters [18,20] are $14\%/\sqrt{E_T} \oplus 2\%$ (CEM) and $16\%/\sqrt{E} \oplus 1\%$ (PEM), where the energies are expressed in GeV. The single-pion energy resolutions in the hadronic calorimeters, as determined in test-beam data

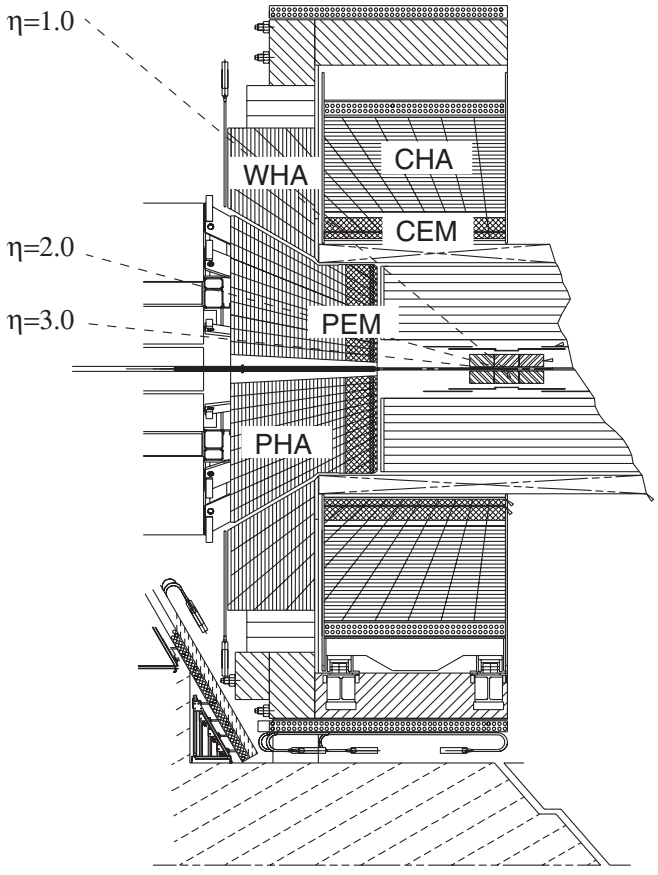

FIG. 1. Elevation view of one-half of the CDF detector displaying the components of the CDF calorimeter.

[18–20], are $50\%/\sqrt{E_T} \oplus 3\%$ (CHA), $75\%/\sqrt{E_T} \oplus 4\%$ (WHA), and $80\%/\sqrt{E} \oplus 5\%$ (PHA). Cherenkov counters covering the $3.7 < |\eta| < 4.7$ region [21] measure the average number of inelastic $p\bar{p}$ collisions per bunch crossing and thereby determine the beam luminosity.

III. JET RECONSTRUCTION

The k_T algorithm [9] is used to reconstruct jets from the energy depositions in the calorimeter towers in both data and Monte Carlo simulated events (see Sec. VI). For each calorimeter tower, the four-momenta [22] of its electromagnetic and hadronic sections are summed to define a physics tower. First, all physics towers with transverse momentum above 0.1 GeV/c are considered as protojets. The quantities

$$k_{T,i} = p_{T,i}^2; \qquad k_{T,(i,j)} = \min(p_{T,i}^2, p_{T,j}^2)\Delta R_{i,j}^2/D^2 \quad (1)$$

are computed for each protojet and pair of protojets, respectively, where $p_{T,i}$ denotes the transverse momentum of the ith protojet, $\Delta R_{i,j}$ is the distance ($y - \phi$ space) between each pair of protojets, and D is a parameter that approximately controls the size of the jet by limiting, in each iteration, the clustering of protojets according to their spacial separation. All $k_{T,i}$ and $k_{T,(i,j)}$ values are then collected into a single sorted list. In this list, if the smallest quantity is of the type $k_{T,i}$, the corresponding protojet is promoted to be a jet and removed from the list. Otherwise, if the smallest quantity is of the type $k_{T,(i,j)}$, the protojets are combined into a single protojet by summing up their four-vector components. The procedure is iterated over protojets until the list is empty. The jet transverse momentum, rapidity, and azimuthal angle are denoted as $p_{T,cal}^{jet}$, y_{cal}^{jet}, and ϕ_{cal}^{jet}, respectively.

In the Monte Carlo event samples, the same jet algorithm is also applied to the final-state particles, considering all particles as protojets, to search for jets at the hadron level. The resulting hadron-level jet variables are denoted as $p_{T,had}^{jet}$, y_{had}^{jet}, and ϕ_{had}^{jet}.

IV. EVENT SELECTION

Events are selected online using a three-level trigger system [23] with unique sets of selection criteria called paths. For the different trigger paths used in this measurement, this selection is based on the measured energy deposits in the calorimeter towers, with different thresholds on the jet E_T and different prescale factors [24] (see Table I). In the first-level trigger, a single trigger tower [25] with E_T above 5 or 10 GeV, depending on the trigger path, is required. In the second-level trigger, calorimeter clusters are formed around the selected trigger towers. The events are required to have at least one second-level trigger cluster with E_T above a given threshold, which varies between 15 and 90 GeV for the different trigger paths. In the third-level trigger, jets are reconstructed using the CDF run I cone algorithm [26], and the events are required to have at least one jet with E_T above 20 to 100 GeV.

Jets are then reconstructed using the k_T algorithm, as explained in Sec. III, with $D = 0.7$. For each trigger path, the minimum $p_{T,cal}^{jet}$, in each $|y_{cal}^{jet}|$ region, is chosen in such a way that the trigger selection is more than 99% efficient. The efficiency for a given trigger path is obtained using events from a different trigger path with lower transverse energy thresholds (see Table I). In the case of the JET 20 trigger path, the trigger efficiency is extracted from additional control samples, which include a sample with only first-level trigger requirements as well as data collected using unbiased trigger paths with no requirement on the energy deposits in the calorimeter towers. As an example, for jets in the region $0.1 < |y_{cal}^{jet}| < 0.7$, Fig. 2 shows the trigger efficiency as a function of $p_{T,cal}^{jet}$ for the different samples. The following selection criteria have been imposed:

(1) Events are required to have at least one reconstructed primary vertex with z-position within 60 cm of the nominal interaction point. This partially removes beam-related backgrounds and ensures a well-understood event-by-event jet kinematics. Primary vertices are reconstructed event-by-event using the tracking system and an algorithm that identifies clusters of tracks pointing to a common z-position along the beam line [27]. In events with more than one reconstructed primary vertex, the one with the highest $\Sigma|p_T^{track}|$ is used to define the kinematics, where $\Sigma|p_T^{track}|$ denotes the scalar sum of the transverse momentum of the tracks associated with the vertex. For the QCD event topologies considered in this analysis, the efficiency for the reconstruction of at least one primary vertex is essentially 100%.

(2) Events are required to have at least one jet with ra-

TABLE I. Summary of trigger paths, trigger thresholds, and effective prescale factors employed to collect the data.

Trigger path	Level 1 tower E_T [GeV]	Level 2 cluster E_T [GeV]	Level 3 jet E_T [GeV]	Effective prescale
JET 20	5	15	20	775
JET 50	5	40	50	34
JET 70	10	60	70	8
JET 100	10	90	100	1

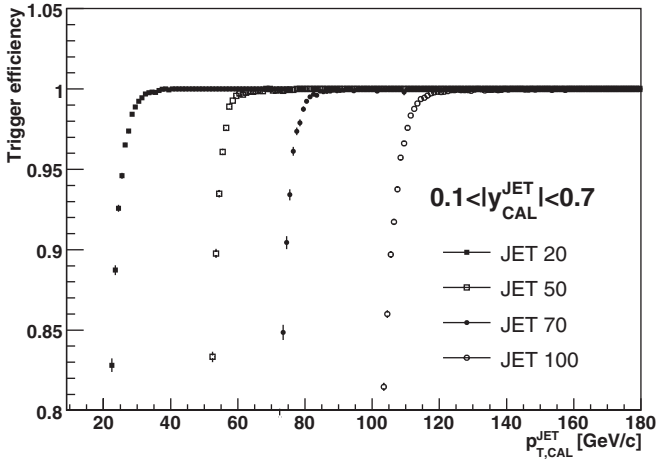

FIG. 2. Measured trigger efficiencies as a function of $p^{\rm jet}_{\rm T,cal}$ for different trigger paths and in the region $0.1 < |y^{\rm jet}_{\rm cal}| < 0.7$. In this particular case, JET 20 trigger path is at least 99% efficient for $p^{\rm jet}_{\rm T,cal} > 32$ GeV$/c$, JET 50 for $p^{\rm jet}_{\rm T,cal} > 60$ GeV$/c$, JET 70 for $p^{\rm jet}_{\rm T,cal} > 84$ GeV$/c$, and JET 100 for $p^{\rm jet}_{\rm T,cal} > 119$ GeV$/c$.

pidity in the region $|y^{\rm jet}_{\rm cal}| < 2.1$ and corrected $p^{\rm jet}_{\rm T,cal}$ (see Sec. IX) above 54 GeV$/c$, which constitutes the minimum jet transverse momentum considered in the analysis. The measurements are limited to jets with $|y^{\rm jet}_{\rm cal}| < 2.1$ to avoid contributions from the p and $\bar{p}$ remnants that would affect the measured $p^{\rm jet}_{\rm T,cal}$ in the most forward region of the calorimeter.

(3) In order to remove beam-related backgrounds and cosmic rays, the events are required to fulfill $\not\!\!E_{\rm T}/\sqrt{\Sigma E_{\rm T}} < F(p^{\rm jet\,1}_{\rm T,cal})$, where $\not\!\!E_{\rm T}$ denotes the missing transverse energy [28] in GeV and $\Sigma E_{\rm T} = \sum_i E^i_{\rm T}$ is the total transverse energy of the event, as measured using calorimeter towers with $E^i_{\rm T}$ above 0.1 GeV. The threshold function $F(p^{\rm jet\,1}_{\rm T,cal})$ is defined as $F(p^{\rm jet}_{\rm T}) = \min(2 + 0.0125 \times p^{\rm jet}_{\rm T}, 7)$, where $p^{\rm jet\,1}_{\rm T,cal}$ is the uncorrected transverse momentum of the leading jet (highest $p^{\rm jet}_{\rm T}$) in GeV$/c$, and F is in GeV$^{1/2}$. This criterion preserves more than 95% of the QCD events, as determined from Monte Carlo studies (see Sec. VI). A visual scan of events with $p^{\rm jet}_{\rm T,cal} >$ 400 GeV$/c$ did not show remaining backgrounds.

Measurements are carried out in five different jet rapidity regions: $|y^{\rm jet}_{\rm cal}| < 0.1$, $0.1 < |y^{\rm jet}_{\rm cal}| < 0.7$, $0.7 < |y^{\rm jet}_{\rm cal}| < 1.1$, $1.1 < |y^{\rm jet}_{\rm cal}| < 1.6$, and $1.6 < |y^{\rm jet}_{\rm cal}| < 2.1$, where the different boundaries are chosen to reduce systematic effects coming from the layout of the calorimeter system.

V. EFFECT OF MULTIPLE $p\bar{p}$ INTERACTIONS

The measured $p^{\rm jet}_{\rm T,cal}$ includes contributions from multiple $p\bar{p}$ interactions per bunch crossing at high instantaneous luminosity, $\mathcal{L}^{\rm inst}$. The data used in this measurement were collected at $\mathcal{L}^{\rm inst}$ between 0.2×10^{31} cm^{-2} s^{-1} and 16.3×10^{31} cm^{-2} s^{-1} with an average of 4.1×10^{31} cm^{-2} s^{-1}. On average, 1.5 inelastic $p\bar{p}$ interactions per bunch crossing are expected. At the highest $\mathcal{L}^{\rm inst}$ considered, an average of 5.9 interactions per bunch crossing are produced. This mainly affects the measured cross section at low $p^{\rm jet}_{\rm T}$ where the contributions are sizable. Multiple interactions are identified via the presence of additional primary vertices reconstructed from charged particles. The measured jet transverse momenta are corrected for this effect by removing a certain amount of transverse momentum, $\delta^{\rm mi}_{p_{\rm T}} \times (N_{\rm V} - 1)$, where $N_{\rm V}$ denotes the number of reconstructed primary vertices in the event and $\delta^{\rm mi}_{p_{\rm T}}$ is determined from the data by requiring that, after the correction is applied, the ratio of cross sections at low and high $\mathcal{L}^{\rm inst}$ does not show any $p^{\rm jet}_{\rm T}$ dependence. The study is carried out separately in each $|y^{\rm jet}_{\rm cal}|$ region, and the results are consistent with a common value $\delta^{\rm mi}_{p_{\rm T}} = 1.86 \pm 0.23$ GeV$/c$ across the whole rapidity range.

VI. MONTE CARLO SIMULATION

Monte Carlo simulated event samples are used to determine the response of the detector and the correction factors to the hadron level. The generated samples are passed through a full CDF II detector simulation (based on GEANT3 [29], where the GFLASH [30] package is used to simulate the energy deposition in the calorimeters) and then reconstructed and analyzed using the same analysis chain as used for the data.

Samples of simulated inclusive jet events have been generated with PYTHIA 6.203 [31] and HERWIG 6.4 [32] Monte Carlo generators, using CTEQ5L [33] PDFs. The PYTHIA samples have been created using a specially tuned set of parameters, denoted as PYTHIA-TUNE A [34], that includes enhanced contributions from initial-state gluon radiation and secondary parton interactions between remnants. The parameters were determined from dedicated studies of the underlying event using the CDF run I data [35] and has been shown to properly describe the measured jet shapes in run II [36]. In the case of PYTHIA, fragmentation into hadrons is carried out using the string model [37] as implemented in JETSET [38], while HERWIG implements the cluster model [39].

VII. SIMULATION OF THE CALORIMETER RESPONSE TO JETS

Dedicated studies have been performed to validate the Monte Carlo simulation of the calorimeter response to jets for the different $|y^{\rm jet}_{\rm cal}|$ regions. Previous analyses [3] for jets with $0.1 < |y^{\rm jet}_{\rm cal}| < 0.7$ indicate that the simulation properly reproduces both the average $p^{\rm jet}_{\rm T}$ and the jet momentum resolution, $\sigma_{p^{\rm jet}_{\rm T}}$, as measured in the data. The study is performed for the rest of the $|y^{\rm jet}_{\rm cal}|$ regions using jets in the

range $0.1 < |y^{\rm jet}_{\rm cal}| < 0.7$ as a reference. An exclusive dijet sample is selected, in data and simulated events, with the following criteria:

(1) Events are required to have one and only one reconstructed primary vertex with z-position within 60 cm of the nominal interaction point.

(2) Events are required to have exactly two jets with $p^{\rm jet}_{\rm T,cal} > 10$ GeV$/c$, where one of the jets must be in the region $0.1 < |y^{\rm jet}_{\rm cal}| < 0.7$.

(3) $\not{E}_{\rm T}/\sqrt{\Sigma E_{\rm T}} < F(p^{\rm jet\,1}_{\rm T,cal})$, as explained in Sec. IV.

The bisector method [40] is applied to data and simulated exclusive dijet events to test the accuracy of the simulated $\sigma_{p^{\rm jet}_{\rm T}}$ in the detector. The study indicates that the simulation systematically underestimates the measured $\sigma_{p^{\rm jet}_{\rm T}}$ by 6% and 10% for jets in the regions $0.7 < |y^{\rm jet}_{\rm cal}| < 1.1$ and $1.6 < |y^{\rm jet}_{\rm cal}| < 2.1$, respectively, with no significant $p^{\rm jet}_{\rm T,cal}$ dependence. An additional smearing of the reconstructed $p^{\rm jet}_{\rm T,cal}$ is applied to the simulated events to account for this effect. In the region $1.1 < |y^{\rm jet}_{\rm cal}| < 1.6$, $\sigma_{p^{\rm jet}_{\rm T}}$ is overestimated by 5% in the simulation. The effect on the final result is included via slightly modified unfolding factors (see Sec. IX). For jets with $|y^{\rm jet}_{\rm cal}| < 0.1$, the simulation properly describes the measured $\sigma_{p^{\rm jet}_{\rm T}}$. Figure 3 shows the ratio between $\sigma_{p^{\rm jet}_{\rm T}}$ in data and simulated events, $\sigma^{\rm data}_{p^{\rm jet}_{\rm T}}/\sigma^{\rm mc}_{p^{\rm jet}_{\rm T}}$, in different $|y^{\rm jet}_{\rm cal}|$ regions as a function of the average $p^{\rm jet}_{\rm T,cal}$ of the dijet event [41]. After corrections have been applied to the simulated events, data and simulation agree. In the region $1.1 < |y^{\rm jet}_{\rm cal}| < 1.6$, and only for the purpose of presentation, a 5% smearing of the reconstructed $p^{\rm jet}_{\rm T,cal}$ is applied to the data to show the resulting good agreement with the uncorrected simulated resolution. The relative difference between data and simulated resolutions is conservatively taken to be $\pm 8\%$ (see Fig. 3) over the whole range in $p^{\rm jet}_{\rm T,cal}$ and $|y^{\rm jet}_{\rm cal}|$ in the evaluation of systematic uncertainties.

The average jet momentum calorimeter response in the simulation is then tested by comparing the $p^{\rm jet}_{\rm T,cal}$ balance in data and simulated exclusive dijet events. The variable β, defined as [42]

$$\beta = \frac{1 + \langle \Delta \rangle}{1 - \langle \Delta \rangle}, \qquad \text{with } \Delta = \frac{p^{\rm test\,jet}_{\rm T,cal} - p^{\rm ref.\,jet}_{\rm T,cal}}{p^{\rm test\,jet}_{\rm T,cal} + p^{\rm ref.\,jet}_{\rm T,cal}}, \qquad (2)$$

is computed in data and simulated events in bins of $(p^{\rm test\,jet}_{\rm T,cal} + p^{\rm ref.\,jet}_{\rm T,cal})/2$, where $p^{\rm ref.\,jet}_{\rm T,cal}$ denotes the transverse momentum of the jet in the region $0.1 < |y^{\rm jet}_{\rm cal}| < 0.7$, and $p^{\rm ref.\,jet}_{\rm T,cal}$ is the transverse momentum of the jet in the $|y^{\rm jet}_{\rm cal}|$ region under study. The presence of calorimeter gaps at $|\eta| \approx 0$ and $|\eta| \approx 1.1$ (see Sec. II) translates into a reduced average calorimeter response to jets. For jets in the regions $|y^{\rm jet}_{\rm cal}| \approx 0$ and $|y^{\rm jet}_{\rm cal}| \approx 1.1$, the value for β is about 0.87. Figure 4 presents the ratios $\beta_{\rm data}/\beta_{\rm mc}$ as a function of $p^{\rm jet}_{\rm T,cal} = p^{\rm test\,jet}_{\rm T,cal}$ in the different $|y^{\rm jet}_{\rm cal}|$ bins considered in the analysis. The study indicates that small corrections are required around calorimeter gaps, $|y^{\rm jet}_{\rm cal}| < 0.1$ and $1.1 < |y^{\rm jet}_{\rm cal}| < 1.6$, as well as in the most forward region,

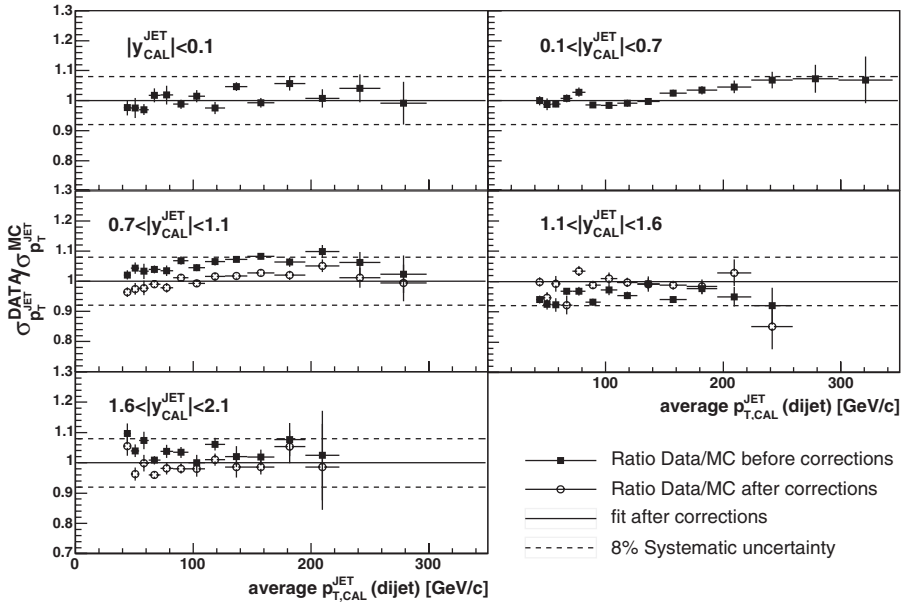

FIG. 3. Ratio $\sigma^{\rm data}_{p^{\rm jet}_{\rm T}}/\sigma^{\rm mc}_{p^{\rm jet}_{\rm T}}$ as a function of the average $p^{\rm jet}_{\rm T,cal}$ of the dijet event, in different $|y^{\rm jet}_{\rm cal}|$ regions, before (black squares) and after (open circles) corrections have been applied (see Sec. VII). The solid lines are fits to the corrected ratios. The dashed lines indicate a $\pm 8\%$ relative variation considered in the study of systematic uncertainties.

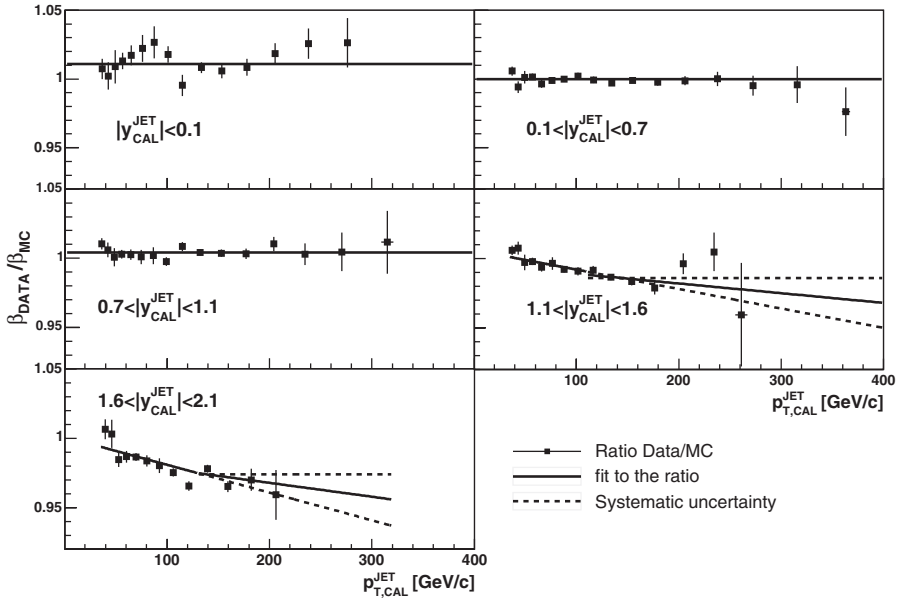

FIG. 4. Ratio $\beta_{\mathrm{data}}/\beta_{\mathrm{mc}}$ as a function of $p^{\mathrm{jet}}_{\mathrm{T,cal}}$ in different $|y^{\mathrm{jet}}_{\mathrm{cal}}|$ regions. The solid lines show the nominal parametrizations based on fits to the ratios. In the region $|y^{\mathrm{jet}}_{\mathrm{cal}}| > 1.1$, the dashed lines indicate different parametrizations used to describe the ratios at high $p^{\mathrm{jet}}_{\mathrm{T,cal}}$, and are considered in the study of systematic uncertainties.

$1.6 < |y^{\mathrm{jet}}_{\mathrm{cal}}| < 2.1$. For jets with $|y^{\mathrm{jet}}_{\mathrm{cal}}| > 1.1$, the correction shows a moderate $p^{\mathrm{jet}}_{\mathrm{T,cal}}$ dependence, and several parametrizations are considered to extrapolate to very high $p^{\mathrm{jet}}_{\mathrm{T,cal}}$. The difference observed in the final results, using different parametrizations, is included as part of the total systematic uncertainty.

VIII. RECONSTRUCTION OF THE JET VARIABLES

The jet reconstruction in the detector is studied using Monte Carlo event samples, with modified jet energy response in the calorimeter, as described in the previous section, and pairs of jets at the calorimeter and hadron levels matched in $(y - \phi)$ space by requiring $\sqrt{(y^{\mathrm{jet}}_{\mathrm{cal}} - y^{\mathrm{jet}}_{\mathrm{had}})^2 + (\phi^{\mathrm{jet}}_{\mathrm{cal}} - \phi^{\mathrm{jet}}_{\mathrm{had}})^2} < D$. These studies indicate that the angular variables of a jet are reconstructed with no significant systematic shift and with a resolution better than 0.05 units in y and ϕ at low $p^{\mathrm{jet}}_{\mathrm{T,cal}}$, improving as $p^{\mathrm{jet}}_{\mathrm{T,cal}}$ increases. The measured $p^{\mathrm{jet}}_{\mathrm{T,cal}}$ systematically underestimates that of the hadron-level jet. This is attributed mainly to the noncompensating nature of the calorimeter [18]. For jets with $p^{\mathrm{jet}}_{\mathrm{T,cal}}$ around 50 GeV/c, the jet transverse momentum is reconstructed with an average shift that varies between -9% and -30% and a resolution between 10% and 16%, depending on the $|y^{\mathrm{jet}}_{\mathrm{cal}}|$ region. The jet reconstruction improves as $p^{\mathrm{jet}}_{\mathrm{T,cal}}$ increases. For jets with $p^{\mathrm{jet}}_{\mathrm{T,cal}}$ around 500 GeV/c, the average shift is -7% and the resolution is about 7%.

IX. UNFOLDING

The measured $p^{\mathrm{jet}}_{\mathrm{T,cal}}$ distributions in the different $|y^{\mathrm{jet}}_{\mathrm{cal}}|$ regions are unfolded back to the hadron level using simulated event samples (see Sec. VI), after including the modified jet energy response described in Sec. VII. PYTHIA-TUNE A provides a reasonable description of the different jet and underlying event quantities, and is used to determine the correction factors in the unfolding procedure. In order to avoid any potential bias on the correction factors due to the particular PDF set used during the generation of the simulated samples, which translates into slightly different simulated $p^{\mathrm{jet}}_{\mathrm{T,cal}}$ distributions, the underlying $\hat{p}_t$ spectrum [43] in PYTHIA-TUNE A is reweighted until the Monte Carlo samples accurately follow each of the measured $p^{\mathrm{jet}}_{\mathrm{T,cal}}$ distributions. The unfolding is carried out in two steps.

First, an average correction is computed separately in each jet rapidity region using corresponding matched pairs of jets at the calorimeter and hadron levels. The correlation $\langle p^{\mathrm{jet}}_{\mathrm{T,had}} - p^{\mathrm{jet}}_{\mathrm{T,cal}} \rangle$ versus $\langle p^{\mathrm{jet}}_{\mathrm{T,cal}} \rangle$ (see Fig. 5), computed in bins of $(p^{\mathrm{jet}}_{\mathrm{T,had}} + p^{\mathrm{jet}}_{\mathrm{T,cal}})/2$, is used to extract correction factors which are then applied to the measured jets to obtain the corrected transverse momenta, $p^{\mathrm{jet}}_{\mathrm{T,cor}}$. In each jet rapidity region, a cross section is defined as

$$\frac{d^2\sigma}{dp^{\mathrm{jet}}_{\mathrm{T,cor}} dy^{\mathrm{jet}}_{\mathrm{cal}}} = \frac{1}{\mathcal{L}} \frac{N^{\mathrm{jet}}_{\mathrm{cor}}}{\Delta p^{\mathrm{jet}}_{\mathrm{T,cor}} \Delta y^{\mathrm{jet}}_{\mathrm{cal}}}, \tag{3}$$

where $N^{\mathrm{jet}}_{\mathrm{cor}}$ denotes the number of jets in a given $p^{\mathrm{jet}}_{\mathrm{T,cor}}$ bin, $\Delta p^{\mathrm{jet}}_{\mathrm{T,cor}}$ is the size of the bin, $\Delta y^{\mathrm{jet}}_{\mathrm{cal}}$ denotes the size of the

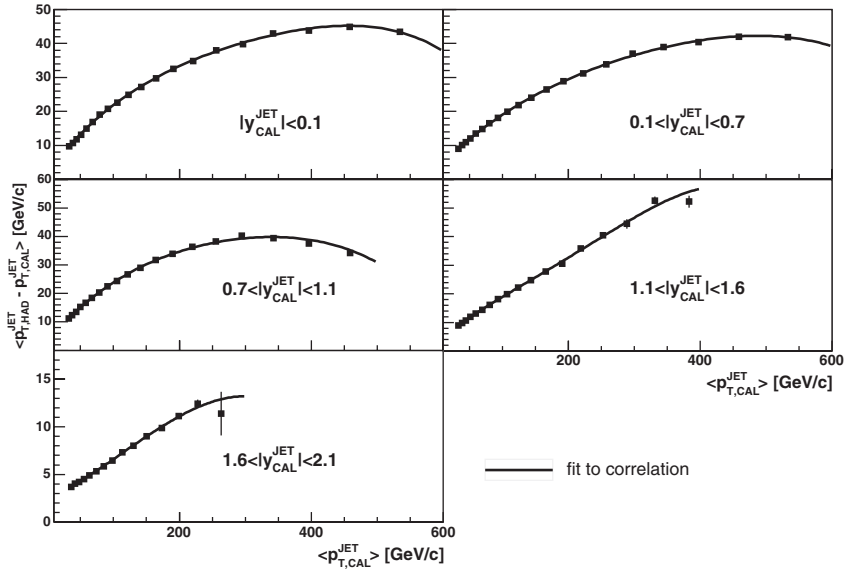

FIG. 5. Correlation $\langle p^{\rm jet}_{\rm T,had} - p^{\rm jet}_{\rm T,cal}\rangle$ versus $\langle p^{\rm jet}_{\rm T,cal}\rangle$, as extracted from PYTHIA-TUNE A simulated event samples, in the different $|y^{\rm jet}_{\rm cal}|$ regions.

region in $y^{\rm jet}_{\rm cal}$, and $\mathcal{L}$ is the integrated luminosity. $N^{\rm jet}_{\rm cor}$ includes event-by-event weights that account for trigger prescale factors, and $\Delta p^{\rm jet}_{\rm T,cor}$ is chosen according to the jet momentum resolution.

Second, each measurement is corrected for acceptance and smearing effects using a bin-by-bin unfolding procedure, which also accounts for the efficiency of the selection criteria. The unfolding factors, defined as

$$U(p^{\rm jet}_{\rm T,cor}, y^{\rm jet}_{\rm cal}) = \frac{d^2\sigma/dp^{\rm jet}_{\rm T,had}dy^{\rm jet}_{\rm had}}{d^2\sigma/dp^{\rm jet}_{\rm T,cor}dy^{\rm jet}_{\rm cal}}, \qquad (4)$$

are extracted from Monte Carlo event samples and applied to the measured $p^{\rm jet}_{\rm T,cor}$ distributions to obtain the final results. As shown in Fig. 6, the factor $U(p^{\rm jet}_{\rm T,cor}, y^{\rm jet}_{\rm cal})$ increases with $p^{\rm jet}_{\rm T,cor}$ and presents a moderate $|y^{\rm jet}_{\rm cal}|$ dependence. At low $p^{\rm jet}_{\rm T,cor}$, the unfolding factor varies between 1.02 and 1.06 for different rapidity regions. For jets with $p^{\rm jet}_{\rm T,cor}$ of about 300 GeV/c, the factor varies between 1.1 and 1.2, and increases up to 1.3–1.4 at very high $p^{\rm jet}_{\rm T,cor}$. In the region $1.1 < |y^{\rm jet}_{\rm cal}| < 1.6$, the unfolding factor includes an additional correction, $f_{\rm U}(p^{\rm jet}_{\rm T,cor})$, to account for the fact that the simulation overestimates the jet momentum resolution in that region (see Sec. VII). The factor $f_{\rm U}(p^{\rm jet}_{\rm T,cor})$ is computed from Monte Carlo samples as the ratio between

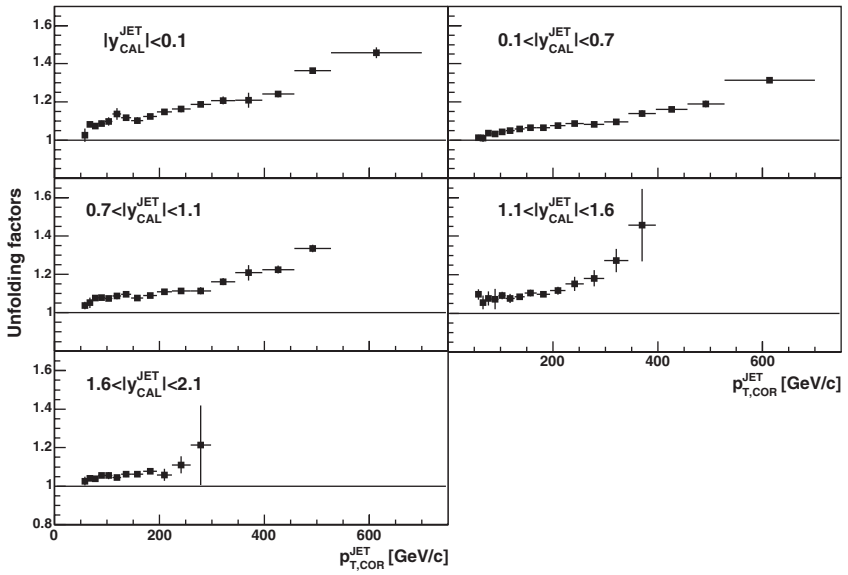

FIG. 6. Unfolding factors, $U(p^{\rm jet}_{\rm T,cor}, y^{\rm jet}_{\rm cal})$, as extracted from PYTHIA-TUNE A simulated event samples, as a function of $p^{\rm jet}_{\rm T,cor}$ in the different $|y^{\rm jet}_{\rm cal}|$ regions.

the $p_{\mathrm{T,had}}^{\mathrm{jet}}$ distribution smeared using the simulated $\sigma_{p_{\mathrm{T}}^{\mathrm{jet}}}$ and the one smeared using $\sigma_{p_{\mathrm{T}}^{\mathrm{jet}}}$ in data as extracted from the bisector method (see Sec. VII). The factor $f_{\mathrm{U}}(p_{\mathrm{T,cor}}^{\mathrm{jet}})$ is about 1.03 and shows no significant $p_{\mathrm{T,cor}}^{\mathrm{jet}}$ dependence.

X. SYSTEMATIC UNCERTAINTIES

A detailed study of the systematic uncertainties on the measurements has been carried out [44]. Tables II and III show the different contributions to the total systematic uncertainty in each $p_{\mathrm{T}}^{\mathrm{jet}}$ bin and $|y^{\mathrm{jet}}|$ region:

TABLE II. Systematic uncertainties (in percent) on the measured inclusive jet differential cross section as a function of $p_{\mathrm{T}}^{\mathrm{jet}}$ for jets in the regions $|y^{\mathrm{jet}}| < 0.1$ and $0.1 < |y^{\mathrm{jet}}| < 0.7$ (see Fig. 7). The different columns follow the discussion in Sec. X. An additional 5.8% uncertainty on the integrated luminosity is not included.

Systematic uncertainties [%] ($\lvert y^{\mathrm{jet}}\rvert < 0.1$)								
		$\beta_{\mathrm{data}}/\beta_{\mathrm{mc}}$						
$p_{\mathrm{T}}^{\mathrm{jet}}$ [GeV/c]	Jet energy scale	(a)	(b)	(c)	Resolution	Unfolding	$p_{\mathrm{T}}^{\mathrm{jet}}$-spectra	$\delta_{p_{\mathrm{T}}}^{\mathrm{mi}}$
54–62	$^{+10.3}_{-9.3}$	$^{+1.4}_{-2.1}$	...	...	$^{+2.8}_{-3.0}$	±8.2	±1.5	$^{+1.8}_{-1.7}$
62–72	$^{+9.9}_{-9.4}$	$^{+1.7}_{-2.1}$	...	...	$^{+2.8}_{-3.0}$	±7.1	±1.4	$^{+1.6}_{-1.5}$
72–83	$^{+9.6}_{-9.4}$	$^{+1.9}_{-2.1}$	...	...	$^{+2.9}_{-3.0}$	±6.2	±1.3	$^{+1.4}_{-1.3}$
83–96	$^{+9.4}_{-9.5}$	$^{+2.1}_{-2.2}$	...	...	$^{+2.9}_{-2.9}$	±5.4	±1.1	$^{+1.3}_{-1.1}$
96–110	$^{+9.5}_{-9.6}$	$^{+2.3}_{-2.2}$	...	...	$^{+2.9}_{-2.9}$	±4.7	±1.0	$^{+1.1}_{-1.0}$
110–127	$^{+9.8}_{-9.8}$	$^{+2.5}_{-2.3}$	...	...	$^{+3.0}_{-2.9}$	±4.2	±0.9	$^{+1.0}_{-0.9}$
127–146	$^{+10.4}_{-10.2}$	$^{+2.7}_{-2.4}$	...	...	$^{+3.1}_{-2.9}$	±3.7	±0.8	$^{+0.9}_{-0.8}$
146–169	$^{+11.2}_{-10.8}$	$^{+2.8}_{-2.6}$	...	...	$^{+3.1}_{-3.0}$	±3.2	±0.6	$^{+0.8}_{-0.8}$
169–195	$^{+12.4}_{-11.6}$	$^{+2.9}_{-2.7}$	...	...	$^{+3.3}_{-3.0}$	±2.8	±0.5	$^{+0.7}_{-0.7}$
195–224	$^{+13.9}_{-12.8}$	$^{+3.0}_{-2.9}$	...	...	$^{+3.4}_{-3.2}$	±2.5	±0.4	$^{+0.6}_{-0.7}$
224–259	$^{+15.5}_{-14.3}$	$^{+3.1}_{-3.1}$	...	...	$^{+3.7}_{-3.4}$	±2.2	±0.3	$^{+0.6}_{-0.6}$
259–298	$^{+17.4}_{-15.9}$	$^{+3.3}_{-3.4}$	...	...	$^{+4.0}_{-3.6}$	±2.0	±0.4	$^{+0.5}_{-0.6}$
298–344	$^{+19.5}_{-17.4}$	$^{+3.6}_{-3.7}$	...	...	$^{+4.3}_{-4.0}$	±1.8	±0.6	$^{+0.5}_{-0.6}$
344–396	$^{+22.1}_{-19.1}$	$^{+4.0}_{-4.0}$	...	...	$^{+4.8}_{-4.5}$	±1.6	±1.0	$^{+0.4}_{-0.5}$
396–457	$^{+25.7}_{-21.6}$	$^{+4.6}_{-4.4}$	...	...	$^{+5.4}_{-5.1}$	±1.4	±1.8	$^{+0.4}_{-0.5}$
457–527	$^{+31.3}_{-26.3}$	$^{+5.3}_{-5.1}$	...	...	$^{+6.1}_{-5.9}$	±1.3	±3.1	$^{+0.3}_{-0.5}$
527–700	$^{+43.7}_{-32.9}$	$^{+7.3}_{-6.7}$	...	...	$^{+7.4}_{-7.3}$	±1.1	±7.1	$^{+0.3}_{-0.5}$
Systematic uncertainties [%] ($0.1 < \lvert y^{\mathrm{jet}}\rvert < 0.7$)								
		$\beta_{\mathrm{data}}/\beta_{\mathrm{mc}}$						
$p_{\mathrm{T}}^{\mathrm{jet}}$ [GeV/c]	Jet energy scale	(a)	(b)	(c)	Resolution	Unfolding	$p_{\mathrm{T}}^{\mathrm{jet}}$-spectra	$\delta_{p_{\mathrm{T}}}^{\mathrm{mi}}$
54–62	$^{+9.5}_{-9.4}$	...	...	...	$^{+2.2}_{-2.5}$	±5.3	±0.6	$^{+1.6}_{-1.6}$
62–72	$^{+9.4}_{-9.1}$	...	...	...	$^{+2.1}_{-2.4}$	±4.7	±0.6	$^{+1.5}_{-1.4}$
72–83	$^{+9.4}_{-8.9}$	...	...	...	$^{+2.1}_{-2.4}$	±4.1	±0.5	$^{+1.3}_{-1.3}$
83–96	$^{+9.4}_{-8.9}$	...	...	...	$^{+2.0}_{-2.3}$	±3.7	±0.5	$^{+1.2}_{-1.1}$
96–110	$^{+9.6}_{-9.0}$	...	...	...	$^{+2.0}_{-2.2}$	±3.3	±0.5	$^{+1.1}_{-1.0}$
110–127	$^{+10.0}_{-9.3}$	...	...	...	$^{+1.9}_{-2.1}$	±3.0	±0.5	$^{+1.0}_{-0.9}$
127–146	$^{+10.6}_{-9.8}$	...	...	...	$^{+1.9}_{-2.1}$	±2.7	±0.5	$^{+0.9}_{-0.8}$
146–169	$^{+11.4}_{-10.6}$	...	...	...	$^{+1.9}_{-2.0}$	±2.4	±0.4	$^{+0.8}_{-0.8}$
169–195	$^{+12.6}_{-11.7}$	...	...	...	$^{+2.0}_{-2.1}$	±2.2	±0.4	$^{+0.7}_{-0.7}$
195–224	$^{+14.1}_{-13.1}$	...	...	...	$^{+2.1}_{-2.1}$	±2.0	±0.4	$^{+0.7}_{-0.7}$
224–259	$^{+16.0}_{-14.8}$	...	...	...	$^{+2.2}_{-2.3}$	±1.8	±0.3	$^{+0.6}_{-0.6}$
259–298	$^{+18.4}_{-16.7}$	...	...	...	$^{+2.5}_{-2.5}$	±1.7	±0.3	$^{+0.6}_{-0.6}$
298–344	$^{+21.3}_{-18.9}$	...	...	...	$^{+2.8}_{-2.9}$	±1.6	±0.3	$^{+0.5}_{-0.6}$
344–396	$^{+25.1}_{-21.4}$	...	...	...	$^{+3.4}_{-3.5}$	±1.5	±0.5	$^{+0.5}_{-0.5}$
396–457	$^{+30.3}_{-24.7}$	...	...	...	$^{+4.1}_{-4.2}$	±1.4	±0.8	$^{+0.4}_{-0.5}$
457–527	$^{+37.7}_{-29.3}$	...	...	...	$^{+5.1}_{-5.2}$	±1.3	±1.4	$^{+0.4}_{-0.5}$
527–700	$^{+52.3}_{-39.8}$	...	...	...	$^{+7.3}_{-7.3}$	±1.2	±3.6	$^{+0.4}_{-0.5}$

TABLE III. Systematic uncertainties (in percent) on the measured inclusive jet differential cross section as a function of p_T^{jet} for jets in the regions $0.7 < |y^{jet}| < 1.1$, $1.1 < |y^{jet}| < 1.6$, and $1.6 < |y^{jet}| < 2.1$ (see Fig. 7). The different columns follow the discussion in Sec. X. An additional 5.8% uncertainty on the integrated luminosity is not included.

Systematic uncertainties [%] ($0.7 < |y^{jet}| < 1.1$)

p_T^{jet} [GeV/c]	Jet energy scale	β_{data}/β_{mc} (a)	(b)	(c)	Resolution	Unfolding	p_T^{jet}-spectra	$\delta^{mi}_{p_T}$
54–62	$^{+9.2}_{-9.9}$	$^{+2.1}_{-2.3}$	…	…	$^{+4.0}_{-3.8}$	±6.3	±2.0	$^{+1.7}_{-1.6}$
62–72	$^{+9.2}_{-9.3}$	$^{+2.2}_{-2.3}$	…	…	$^{+3.8}_{-3.7}$	±5.6	±1.9	$^{+1.5}_{-1.4}$
72–83	$^{+9.2}_{-9.0}$	$^{+2.3}_{-2.3}$	…	…	$^{+3.7}_{-3.5}$	±4.9	±1.8	$^{+1.3}_{-1.3}$
83–96	$^{+9.5}_{-9.0}$	$^{+2.3}_{-2.3}$	…	…	$^{+3.5}_{-3.4}$	±4.4	±1.8	$^{+1.2}_{-1.2}$
96–110	$^{+9.9}_{-9.3}$	$^{+2.4}_{-2.4}$	…	…	$^{+3.4}_{-3.3}$	±3.9	±1.7	$^{+1.1}_{-1.1}$
110–127	$^{+10.6}_{-9.8}$	$^{+2.5}_{-2.5}$	…	…	$^{+3.3}_{-3.2}$	±3.5	±1.7	$^{+1.0}_{-1.0}$
127–146	$^{+11.5}_{-10.7}$	$^{+2.6}_{-2.6}$	…	…	$^{+3.3}_{-3.1}$	±3.2	±1.7	$^{+0.9}_{-0.9}$
146–169	$^{+12.6}_{-11.7}$	$^{+2.8}_{-2.7}$	…	…	$^{+3.3}_{-3.2}$	±2.8	±1.6	$^{+0.8}_{-0.8}$
169–195	$^{+14.1}_{-13.0}$	$^{+3.0}_{-2.9}$	…	…	$^{+3.4}_{-3.3}$	±2.6	±1.6	$^{+0.8}_{-0.8}$
195–224	$^{+15.9}_{-14.6}$	$^{+3.3}_{-3.2}$	…	…	$^{+3.7}_{-3.5}$	±2.3	±1.7	$^{+0.7}_{-0.7}$
224–259	$^{+18.1}_{-16.5}$	$^{+3.8}_{-3.6}$	…	…	$^{+4.1}_{-3.9}$	±2.1	±1.8	$^{+0.7}_{-0.7}$
259–298	$^{+21.0}_{-19.2}$	$^{+4.4}_{-4.1}$	…	…	$^{+4.7}_{-4.5}$	±2.0	±2.1	$^{+0.6}_{-0.6}$
298–344	$^{+25.2}_{-22.7}$	$^{+5.0}_{-4.8}$	…	…	$^{+5.6}_{-5.3}$	±1.8	±2.4	$^{+0.6}_{-0.6}$
344–396	$^{+31.5}_{-26.9}$	$^{+5.9}_{-5.6}$	…	…	$^{+6.8}_{-6.4}$	±1.7	±3.0	$^{+0.6}_{-0.6}$
396–457	$^{+41.3}_{-31.0}$	$^{+7.2}_{-6.6}$	…	…	$^{+8.3}_{-7.7}$	±1.6	±3.8	$^{+0.5}_{-0.5}$
457–527	$^{+55.4}_{-38.3}$	$^{+10.4}_{-7.7}$	…	…	$^{+10.0}_{-9.1}$	±1.5	±5.0	$^{+0.5}_{-0.5}$

Systematic uncertainties [%] ($1.1 < |y^{jet}| < 1.6$)

p_T^{jet} [GeV/c]	Jet energy scale	β_{data}/β_{mc} (a)	(b)	(c)	Resolution	Unfolding	p_T^{jet}-spectra	$\delta^{mi}_{p_T}$
54–62	$^{+9.4}_{-8.6}$	$^{+2.6}_{-2.4}$	…	$^{+0.0}_{-3.0}$	$^{+2.9}_{-3.1}$	±6.7	±1.3	$^{+1.8}_{-1.8}$
62–72	$^{+9.5}_{-8.9}$	$^{+2.5}_{-2.4}$	…	$^{+0.0}_{-3.0}$	$^{+2.9}_{-3.0}$	±6.4	±1.1	$^{+1.6}_{-1.5}$
72–83	$^{+9.8}_{-9.3}$	$^{+2.5}_{-2.5}$	…	$^{+0.0}_{-3.0}$	$^{+2.9}_{-2.9}$	±6.1	±0.9	$^{+1.4}_{-1.3}$
83–96	$^{+10.2}_{-9.8}$	$^{+2.5}_{-2.6}$	…	$^{+0.0}_{-3.0}$	$^{+2.9}_{-2.8}$	±5.8	±0.8	$^{+1.3}_{-1.2}$
96–110	$^{+10.9}_{-10.5}$	$^{+2.6}_{-2.6}$	…	$^{+0.0}_{-3.0}$	$^{+3.0}_{-2.9}$	±5.6	±0.6	$^{+1.2}_{-1.1}$
110–127	$^{+11.7}_{-11.4}$	$^{+2.7}_{-2.8}$	…	$^{+0.0}_{-3.0}$	$^{+3.1}_{-3.0}$	±5.4	±0.4	$^{+1.1}_{-1.0}$
127–146	$^{+12.8}_{-12.6}$	$^{+2.9}_{-3.0}$	…	$^{+0.0}_{-3.0}$	$^{+3.4}_{-3.2}$	±5.2	±0.3	$^{+1.1}_{-1.0}$
146–169	$^{+14.5}_{-14.2}$	$^{+3.3}_{-3.3}$	…	$^{+0.0}_{-3.0}$	$^{+3.8}_{-3.6}$	±5.0	±0.1	$^{+1.0}_{-0.9}$
169–195	$^{+16.9}_{-16.2}$	$^{+3.8}_{-3.7}$	…	$^{+0.0}_{-3.0}$	$^{+4.3}_{-4.2}$	±4.8	±0.1	$^{+1.0}_{-0.9}$
195–224	$^{+20.3}_{-18.6}$	$^{+4.4}_{-4.2}$	$^{+0.7}_{-0.9}$	$^{+0.0}_{-3.0}$	$^{+5.1}_{-5.0}$	±4.7	±0.2	$^{+0.9}_{-0.9}$
224–259	$^{+24.7}_{-21.2}$	$^{+5.2}_{-5.0}$	$^{+2.6}_{-2.4}$	$^{+0.0}_{-3.0}$	$^{+6.2}_{-6.1}$	±4.6	±0.4	$^{+0.9}_{-0.9}$
259–298	$^{+29.9}_{-24.1}$	$^{+6.2}_{-5.9}$	$^{+6.3}_{-4.5}$	$^{+0.0}_{-3.0}$	$^{+7.8}_{-7.3}$	±4.4	±0.8	$^{+0.9}_{-0.9}$
298–344	$^{+37.2}_{-28.6}$	$^{+7.3}_{-7.1}$	$^{+12.6}_{-7.5}$	$^{+0.0}_{-3.0}$	$^{+9.8}_{-8.5}$	±4.3	±1.6	$^{+0.9}_{-0.9}$
344–396	$^{+61.2}_{-39.2}$	$^{+8.7}_{-8.3}$	$^{+22.7}_{-11.7}$	$^{+0.0}_{-3.0}$	$^{+12.4}_{-9.4}$	±4.2	±2.8	$^{+0.9}_{-0.9}$

Systematic uncertainties [%] ($1.6 < |y^{jet}| < 2.1$)

p_T^{jet} [GeV/c]	Jet energy scale	β_{data}/β_{mc} (a)	(b)	(c)	Resolution	Unfolding	p_T^{jet}-spectra	$\delta^{mi}_{p_T}$
54–62	$^{+11.6}_{-10.3}$	$^{+2.3}_{-2.1}$	…	…	$^{+1.7}_{-1.6}$	±3.2	±1.0	$^{+2.1}_{-2.0}$
62–72	$^{+10.9}_{-10.1}$	$^{+2.4}_{-2.4}$	…	…	$^{+1.6}_{-1.7}$	±3.3	±0.8	$^{+1.8}_{-1.8}$
72–83	$^{+11.0}_{-10.3}$	$^{+2.6}_{-2.6}$	…	…	$^{+1.5}_{-1.7}$	±3.4	±0.6	$^{+1.7}_{-1.7}$
83–96	$^{+12.0}_{-11.1}$	$^{+2.8}_{-2.9}$	…	…	$^{+1.5}_{-1.8}$	±3.5	±0.4	$^{+1.6}_{-1.6}$
96–110	$^{+13.7}_{-12.5}$	$^{+3.2}_{-3.2}$	…	…	$^{+1.5}_{-1.8}$	±3.6	±0.3	$^{+1.5}_{-1.5}$
110–127	$^{+16.2}_{-14.4}$	$^{+3.7}_{-3.5}$	…	…	$^{+1.6}_{-1.9}$	±3.7	±0.2	$^{+1.4}_{-1.4}$
127–146	$^{+19.2}_{-16.9}$	$^{+4.3}_{-4.0}$	…	…	$^{+1.8}_{-2.0}$	±3.7	±0.1	$^{+1.4}_{-1.4}$
146–169	$^{+22.8}_{-19.8}$	$^{+5.0}_{-4.6}$	…	…	$^{+2.1}_{-2.1}$	±3.8	±0.2	$^{+1.4}_{-1.3}$
169–195	$^{+27.7}_{-23.0}$	$^{+6.0}_{-5.4}$	$^{+1.3}_{-0.9}$	…	$^{+2.5}_{-2.3}$	±3.8	±0.5	$^{+1.4}_{-1.3}$
195–224	$^{+34.9}_{-26.7}$	$^{+7.0}_{-6.4}$	$^{+5.3}_{-5.6}$	…	$^{+3.0}_{-2.7}$	±3.8	±1.1	$^{+1.4}_{-1.3}$
224–259	$^{+46.0}_{-32.4}$	$^{+8.1}_{-8.0}$	$^{+11.0}_{-11.1}$	…	$^{+3.5}_{-3.3}$	±3.8	±2.1	$^{+1.4}_{-1.3}$
259–298	$^{+52.9}_{-44.5}$	$^{+9.1}_{-10.5}$	$^{+19.1}_{-17.5}$	…	$^{+3.9}_{-4.4}$	±3.8	±3.7	$^{+1.4}_{-1.3}$

(1) The measured jet energies are varied by $\pm 2\%$ at low p_T^{jet} to $\pm 2.7\%$ at high p_T^{jet} to account for the uncertainty on the absolute energy scale [45] in the calorimeter (see also Appendix A). This introduces an uncertainty on the measured cross sections which varies between $\pm 9\%$ at low p_T^{jet} and $^{+61\%}_{-39\%}$ at high p_T^{jet}, and dominates the total systematic uncertainty on the different measurements.

(2) Several sources of systematic uncertainty on the ratio β_{data}/β_{mc} are considered for the different $|y^{jet}|$ regions:
   (a) The uncertainty on the definition of the exclusive dijet sample in data and Monte Carlo events introduces a $\pm 0.5\%$ uncertainty on the absolute energy scale for jets outside the region $0.1 < |y^{jet}| < 0.7$, which translates into an uncertainty on the cross sections between $\pm 2\%$ at low p_T^{jet} and $\pm 10\%$ at very high p_T^{jet}.
   (b) The use of different β_{data}/β_{mc} parametrizations for jets with $|y^{jet}| > 1.1$ introduces uncertainties between 12% and 23% at very high p_T^{jet}.
   (c) In the region $1.1 < |y^{jet}| < 1.6$, an additional $^{+0\%}_{-3\%}$ uncertainty on the measured cross sections, independent of p_T^{jet}, accounts for variations in the β_{data}/β_{mc} ratio due to the overestimation of the jet momentum resolution in the simulated samples.

(3) A $\pm 8\%$ uncertainty on the jet momentum resolution introduces an uncertainty between $\pm 2\%$ at low p_T^{jet} and $^{+12\%}_{-9\%}$ at high p_T^{jet}.

(4) The unfolding procedure is repeated using HERWIG instead of PYTHIA-TUNE A to account for the uncertainty on the modeling of the parton cascades and the jet fragmentation into hadrons. This translates into an uncertainty on the measured cross sections between $\pm 3\%$ and $\pm 8\%$ at low p_T^{jet} that becomes negligible at very high p_T^{jet}.

(5) The unfolding procedure is also carried out using unweighted PYTHIA-TUNE A, to estimate the residual dependence on the p_T^{jet} spectra. This introduces an uncertainty of about $\pm 3\%$ to $\pm 7\%$ at very high p_T^{jet}, which becomes negligible at low p_T^{jet}.

(6) The quoted ± 0.23 GeV$/c$ uncertainty on $\delta^{mi}_{p_T}$ is taken into account. The maximal effect on the measured cross sections is about $\pm 2\%$.

(7) Different sources of systematic uncertainty related to the selection criteria are considered. The threshold on the z-position of the primary vertex is varied by ± 5 cm in data and simulated events. The lower edge of each $p_{T,cal}^{jet}$ bin is varied by $\pm 3\%$ in data and simulated events. The $\not\!\!E_T$ scale is varied by $\pm 10\%$ in the data. The total effect on the measured cross sections is smaller than 1% and considered negligible.

Positive and negative deviations with respect to the nominal values in each p_T^{jet} bin are added separately in quadrature. Figure 7 shows the total systematic uncertainty as a function of p_T^{jet} in the different $|y^{jet}|$ regions, where an additional 5.8% uncertainty on the total luminosity is not included.

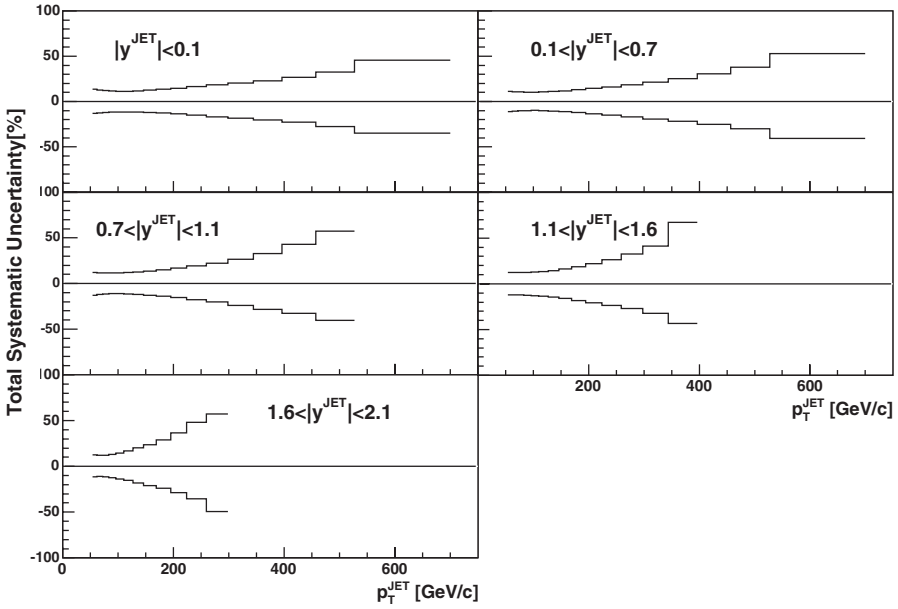

FIG. 7. Total systematic uncertainty (in percent) on the measured inclusive differential jet cross sections as a function p_T^{jet} for the different $|y^{jet}|$ regions (see Tables II and III). An additional 5.8% uncertainty on the integrated luminosity is not included.

XI. QCD PREDICTIONS

The measurements are compared to parton-level NLO pQCD predictions, as computed using JETRAD [11] with CTEQ6.1M PDFs [12] and the renormalization and factorization scales (μ_R and μ_F) both set to $\mu_0 = \max(p_T^{jet})/2$. Different sources of uncertainty on the theoretical predictions are considered. The main contribution comes from the uncertainty on the PDFs and is computed using the Hessian method [46]. At low p_T^{jet}, the uncertainty is about $\pm 5\%$ and approximately independent of y^{jet}. The uncertainty increases as p_T^{jet} and $|y^{jet}|$ increase. At very high p_T^{jet}, the uncertainty varies between $^{+60\%}_{-30\%}$ and $^{+130\%}_{-40\%}$ for jets with $|y^{jet}| < 0.1$ and $1.6 < |y^{jet}| < 2.1$, respectively, and is dominated by the limited knowledge of the gluon PDF. An increase of μ_R and μ_F from μ_0 to $2\mu_0$ changes the theoretical predictions by only a few percent. Values significantly smaller than μ_0 lead to unstable NLO results and are not considered.

The theoretical predictions include a correction factor, $C_{HAD}(p_T^{jet}, y^{jet})$, that approximately accounts for nonperturbative contributions from the underlying event and fragmentation of partons into hadrons (see Fig. 8 and Tables IV and V). In each jet rapidity region, C_{HAD} is estimated, using PYTHIA-TUNE A, as the ratio between the nominal $p_{T,had}^{jet}$ distribution and the one obtained after removing the interactions between p and $\bar{p}$ remnants and the fragmentation into hadrons in the Monte Carlo samples. The correction decreases as p_T^{jet} increases and shows a moderate $|y^{jet}|$ dependence. At low p_T^{jet}, C_{HAD} varies between 1.18 and 1.13 as $|y^{jet}|$ increases, and it becomes of the order of 1.02 at very high p_T^{jet}. The uncertainty on C_{HAD} varies between $\pm 9\%$ and $\pm 12\%$ at low p_T^{jet} and decreases to about $\pm 1\%$ at very high p_T^{jet}, as determined from the difference between the parton-to-hadron correction factors obtained using HERWIG instead of PYTHIA-TUNE A.

XII. RESULTS

The measured inclusive jet cross sections, $d^2\sigma/dp_T^{jet}dy^{jet}$, refer to hadron-level jets, reconstructed using the k_T algorithm with $D = 0.7$, in the region $p_T^{jet} > 54$ GeV/c and $|y^{jet}| < 2.1$. Figure 9 shows the measured cross sections as a function of p_T^{jet} in five different $|y^{jet}|$ regions compared to NLO pQCD predictions. The data are reported in Tables IV and V. The measured cross sections decrease by more than 7 to 8 orders of magnitude as p_T^{jet} increases. Figure 10 shows the ratio data/theory as a function of p_T^{jet} in the five different $|y^{jet}|$ regions. Good agreement is observed in the whole range in p_T^{jet} and y^{jet} between the measured cross sections and the theoretical predictions. In particular, no significant deviation from the pQCD prediction is observed for central jets at high p_T^{jet}. The corresponding χ^2 tests, relative to the nominal pQCD prediction and performed separately in each $|y^{jet}|$ region, give probabilities that vary between 9% and 90%. A global χ^2 test, applied to all the data points in all $|y^{jet}|$ regions simultaneously, gives a probability of 7%. In both cases, a detailed treatment of correlations between systematic uncertainties was considered, as discussed in Appendix A. In addition, Fig. 10 shows the ratio of pQCD predictions using MRST2004 [13] and CTEQ6.1M PDF sets, well inside the theoretical and experimental uncertainties. The

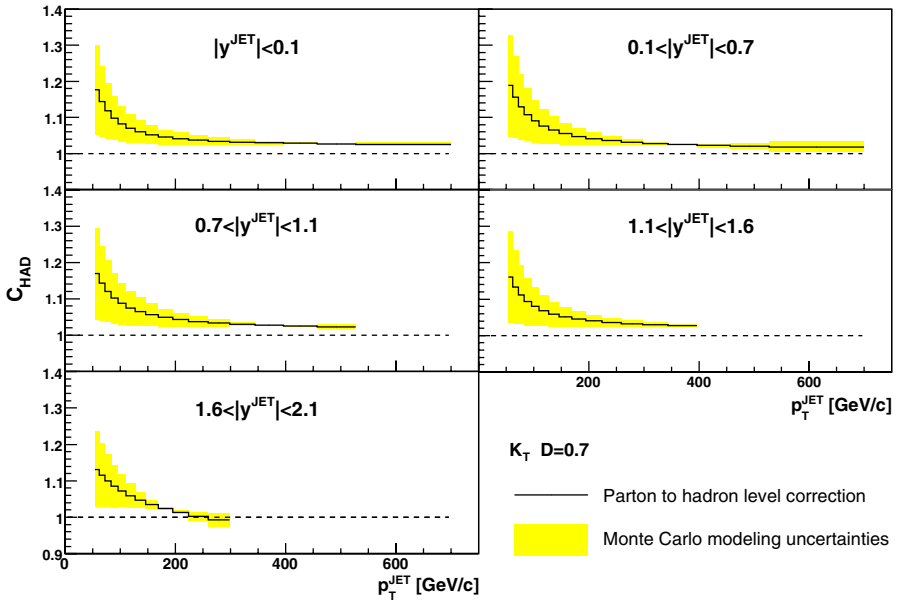

FIG. 8 (color online). Magnitude of the parton-to-hadron correction, $C_{HAD}(p_T^{jet}, y^{jet})$, used to correct the NLO pQCD predictions (see Tables IV and V). The shaded bands indicate the quoted Monte Carlo modeling uncertainty.

TABLE IV. Measured inclusive jet differential cross section as a function of p_T^{jet} for jets in the regions $|y^{jet}| < 0.1$ and $0.1 < |y^{jet}| < 0.7$ (see Fig. 9). An additional 5.8% uncertainty on the integrated luminosity is not included. The parton-to-hadron correction factors, $C_{HAD}(p_T^{jet}, y^{jet})$, are applied to the pQCD predictions (see Fig. 8).

$\frac{d^2\sigma}{dp_T^{jet}dy^{jet}}(\lvert y^{jet}\rvert < 0.1)$		
p_T^{jet} [GeV/c]	$\sigma \pm$ (stat) $\pm$ (sys) [nb/(GeV/c)]	C_{HAD} parton $\rightarrow$ hadron
54–62	$(14.5 \pm 0.5^{+2.0}_{-1.9}) \times 10^{0}$	1.177 ± 0.124
62–72	$(6.68 \pm 0.08^{+0.85}_{-0.84}) \times 10^{0}$	1.144 ± 0.097
72–83	$(2.87 \pm 0.05^{+0.35}_{-0.34}) \times 10^{0}$	1.119 ± 0.077
83–96	$(1.24 \pm 0.02^{+0.14}_{-0.14}) \times 10^{0}$	1.098 ± 0.061
96–110	$(5.31 \pm 0.11^{+0.60}_{-0.61}) \times 10^{-1}$	1.083 ± 0.049
110–127	$(2.33 \pm 0.06^{+0.27}_{-0.26}) \times 10^{-1}$	1.070 ± 0.039
127–146	$(9.36 \pm 0.12^{+1.10}_{-1.08}) \times 10^{-2}$	1.060 ± 0.032
146–169	$(3.63 \pm 0.06^{+0.45}_{-0.43}) \times 10^{-2}$	1.052 ± 0.026
169–195	$(1.39 \pm 0.01^{+0.19}_{-0.18}) \times 10^{-2}$	1.046 ± 0.021
195–224	$(5.22 \pm 0.06^{+0.77}_{-0.72}) \times 10^{-3}$	1.041 ± 0.017
224–259	$(1.79 \pm 0.03^{+0.29}_{-0.27}) \times 10^{-3}$	1.037 ± 0.013
259–298	$(5.92 \pm 0.11^{+1.08}_{-1.00}) \times 10^{-4}$	1.034 ± 0.010
298–344	$(1.78 \pm 0.06^{+0.36}_{-0.33}) \times 10^{-4}$	1.032 ± 0.007
344–396	$(4.68 \pm 0.28^{+1.08}_{-0.94}) \times 10^{-5}$	1.030 ± 0.005
396–457	$(1.29 \pm 0.12^{+0.34}_{-0.29}) \times 10^{-5}$	1.028 ± 0.002
457–527	$(2.47 \pm 0.50^{+0.80}_{-0.68}) \times 10^{-6}$	1.027 ± 0.001
527–700	$(2.13 \pm 0.95^{+0.97}_{-0.75}) \times 10^{-7}$	1.026 ± 0.006
$\frac{d^2\sigma}{dp_T^{jet}dy^{jet}}(0.1 < \lvert y^{jet}\rvert < 0.7)$		
p_T^{jet} [GeV/c]	$\sigma \pm$ (stat) $\pm$ (sys) [nb/(GeV/c)]	C_{HAD} parton $\rightarrow$ hadron
54–62	$(14.0 \pm 0.20^{+1.6}_{-1.6}) \times 10^{0}$	1.188 ± 0.140
62–72	$(6.14 \pm 0.12^{+0.66}_{-0.65}) \times 10^{0}$	1.156 ± 0.113
72–83	$(2.69 \pm 0.02^{+0.29}_{-0.27}) \times 10^{0}$	1.129 ± 0.091
83–96	$(1.14 \pm 0.01^{+0.12}_{-0.11}) \times 10^{0}$	1.108 ± 0.073
96–110	$(4.90 \pm 0.04^{+0.51}_{-0.48}) \times 10^{-1}$	1.090 ± 0.059
110–127	$(2.08 \pm 0.02^{+0.22}_{-0.21}) \times 10^{-1}$	1.076 ± 0.047
127–146	$(8.51 \pm 0.04^{+0.95}_{-0.89}) \times 10^{-2}$	1.065 ± 0.038
146–169	$(3.33 \pm 0.02^{+0.40}_{-0.37}) \times 10^{-2}$	1.055 ± 0.029
169–195	$(1.23 \pm 0.01^{+0.16}_{-0.15}) \times 10^{-2}$	1.047 ± 0.023
195–224	$(4.53 \pm 0.02^{+0.65}_{-0.61}) \times 10^{-3}$	1.041 ± 0.017
224–259	$(1.57 \pm 0.01^{+0.26}_{-0.24}) \times 10^{-3}$	1.036 ± 0.012
259–298	$(4.87 \pm 0.06^{+0.91}_{-0.83}) \times 10^{-4}$	1.031 ± 0.007
298–344	$(1.43 \pm 0.02^{+0.31}_{-0.27}) \times 10^{-4}$	1.028 ± 0.003
344–396	$(3.69 \pm 0.10^{+0.94}_{-0.80}) \times 10^{-5}$	1.025 ± 0.001
396–457	$(7.18 \pm 0.34^{+2.20}_{-1.80}) \times 10^{-6}$	1.023 ± 0.004
457–527	$(1.16 \pm 0.13^{+0.44}_{-0.35}) \times 10^{-6}$	1.021 ± 0.008
527–700	$(8.97 \pm 2.40^{+4.75}_{-3.64}) \times 10^{-8}$	1.018 ± 0.014

TABLE V. Measured inclusive jet differential cross section as a function of p_T^{jet} for jets in the regions $0.7 < |y^{jet}| < 1.1$, $1.1 < |y^{jet}| < 1.6$, and $1.6 < |y^{jet}| < 2.1$ (see Fig. 9). An additional 5.8% uncertainty on the integrated luminosity is not included. The parton-to-hadron correction factors, $C_{HAD}(p_T^{jet}, y^{jet})$, are applied to the pQCD predictions (see Fig. 8).

$\frac{d^2\sigma}{dp_T^{jet}dy^{jet}}(0.7 < \lvert y^{jet}\rvert < 1.1)$		
p_T^{jet} [GeV/c]	$\sigma \pm$ (stat) $\pm$ (sys) [nb/(GeV/c)]	C_{HAD} parton $\rightarrow$ hadron
54–62	$(12.3 \pm 0.2^{+1.5}_{-1.5}) \times 10^{0}$	1.169 ± 0.125
62–72	$(5.48 \pm 0.14^{+0.65}_{-0.65}) \times 10^{0}$	1.143 ± 0.103
72–83	$(2.40 \pm 0.02^{+0.28}_{-0.27}) \times 10^{0}$	1.120 ± 0.085
83–96	$(1.00 \pm 0.01^{+0.15}_{-0.11}) \times 10^{0}$	1.102 ± 0.070
96–110	$(4.15 \pm 0.05^{+0.48}_{-0.46}) \times 10^{-1}$	1.087 ± 0.057
110–127	$(1.73 \pm 0.03^{+0.21}_{-0.20}) \times 10^{-1}$	1.075 ± 0.047
127–146	$(6.83 \pm 0.05^{+0.87}_{-0.82}) \times 10^{-2}$	1.064 ± 0.038
146–169	$(2.52 \pm 0.03^{+0.35}_{-0.33}) \times 10^{-2}$	1.056 ± 0.031
169–195	$(8.95 \pm 0.06^{+1.36}_{-1.26}) \times 10^{-3}$	1.048 ± 0.024
195–224	$(3.04 \pm 0.02^{+0.51}_{-0.47}) \times 10^{-3}$	1.042 ± 0.019
224–259	$(9.52 \pm 0.11^{+1.82}_{-1.68}) \times 10^{-4}$	1.037 ± 0.014
259–298	$(2.53 \pm 0.05^{+0.56}_{-0.51}) \times 10^{-4}$	1.033 ± 0.009
298–344	$(6.18 \pm 0.17^{+1.64}_{-1.49}) \times 10^{-5}$	1.030 ± 0.005
344–396	$(1.11 \pm 0.07^{+0.36}_{-0.31}) \times 10^{-5}$	1.027 ± 0.001
396–457	$(1.53 \pm 0.20^{+0.65}_{-0.50}) \times 10^{-6}$	1.025 ± 0.003
457–527	$(2.17 \pm 0.72^{+1.25}_{-0.88}) \times 10^{-7}$	1.023 ± 0.007
$\frac{d^2\sigma}{dp_T^{jet}dy^{jet}}(1.1 < \lvert y^{jet}\rvert < 1.6)$		
p_T^{jet} [GeV/c]	$\sigma \pm$ (stat) $\pm$ (sys) [nb/(GeV/c)]	C_{HAD} parton $\rightarrow$ hadron
54–62	$(11.0 \pm 0.3^{+1.4}_{-1.3}) \times 10^{0}$	1.160 ± 0.125
62–72	$(4.40 \pm 0.15^{+0.54}_{-0.53}) \times 10^{0}$	1.133 ± 0.101
72–83	$(1.82 \pm 0.06^{+0.22}_{-0.22}) \times 10^{0}$	1.111 ± 0.081
83–96	$(7.22 \pm 0.37^{+0.90}_{-0.90}) \times 10^{-1}$	1.094 ± 0.065
96–110	$(2.98 \pm 0.05^{+0.38}_{-0.38}) \times 10^{-1}$	1.080 ± 0.052
110–127	$(1.14 \pm 0.03^{+0.15}_{-0.15}) \times 10^{-1}$	1.068 ± 0.042
127–146	$(4.10 \pm 0.04^{+0.60}_{-0.60}) \times 10^{-2}$	1.059 ± 0.034
146–169	$(1.39 \pm 0.02^{+0.22}_{-0.23}) \times 10^{-2}$	1.051 ± 0.027
169–195	$(4.19 \pm 0.04^{+0.78}_{-0.76}) \times 10^{-3}$	1.045 ± 0.021
195–224	$(1.15 \pm 0.02^{+0.25}_{-0.24}) \times 10^{-3}$	1.040 ± 0.016
224–259	$(2.73 \pm 0.09^{+0.73}_{-0.64}) \times 10^{-4}$	1.036 ± 0.012
259–298	$(5.18 \pm 0.23^{+1.68}_{-1.39}) \times 10^{-5}$	1.033 ± 0.009
298–344	$(7.99 \pm 0.61^{+3.31}_{-2.56}) \times 10^{-6}$	1.030 ± 0.006
344–396	$(1.05 \pm 0.22^{+0.71}_{-0.45}) \times 10^{-6}$	1.028 ± 0.003
$\frac{d^2\sigma}{dp_T^{jet}dy^{jet}}(1.6 < \lvert y^{jet}\rvert < 2.1)$		
p_T^{jet} [GeV/c]	$\sigma \pm$ (stat) $\pm$ (sys) [nb/(GeV/c)]	C_{HAD} parton $\rightarrow$ hadron
54–62	$(6.67 \pm 0.15^{+0.84}_{-0.75}) \times 10^{0}$	1.132 ± 0.104
62–72	$(2.68 \pm 0.02^{+0.32}_{-0.30}) \times 10^{0}$	1.116 ± 0.087
72–83	$(1.04 \pm 0.01^{+0.12}_{-0.12}) \times 10^{0}$	1.100 ± 0.072
83–96	$(3.77 \pm 0.04^{+0.49}_{-0.46}) \times 10^{-1}$	1.086 ± 0.058
96–110	$(1.32 \pm 0.02^{+0.19}_{-0.18}) \times 10^{-1}$	1.072 ± 0.045
110–127	$(4.18 \pm 0.04^{+0.72}_{-0.65}) \times 10^{-2}$	1.059 ± 0.033
127–146	$(1.21 \pm 0.02^{+0.24}_{-0.22}) \times 10^{-2}$	1.047 ± 0.022
146–169	$(2.92 \pm 0.04^{+0.70}_{-0.61}) \times 10^{-3}$	1.035 ± 0.012
169–195	$(5.74 \pm 0.09^{+1.65}_{-1.38}) \times 10^{-4}$	1.024 ± 0.003
195–224	$(8.49 \pm 0.31^{+3.09}_{-2.42}) \times 10^{-5}$	1.013 ± 0.005
224–259	$(8.65 \pm 0.63^{+4.18}_{-3.08}) \times 10^{-6}$	1.003 ± 0.012
259–298	$(5.67 \pm 1.65^{+3.25}_{-2.80}) \times 10^{-7}$	0.993 ± 0.018

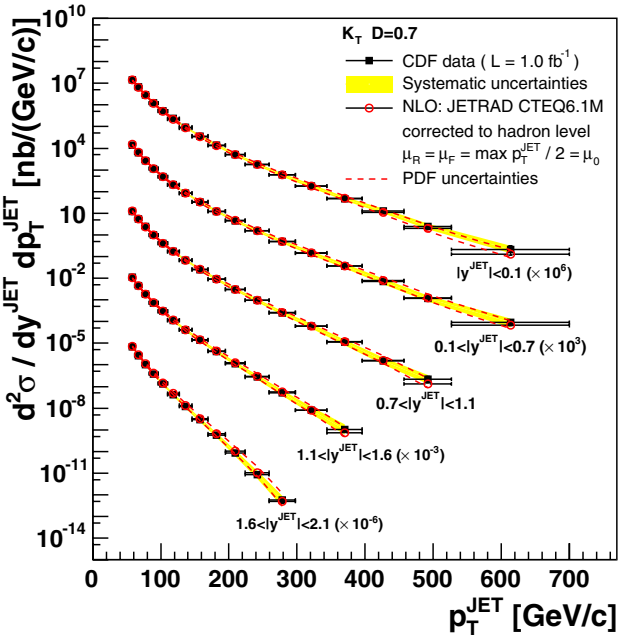

FIG. 9 (color online). Measured inclusive differential jet cross sections (black squares) as a function of p_T^{jet} for jets with $p_T^{jet} > 54$ GeV/c in different $|y^{jet}|$ regions compared to NLO pQCD predictions (open circles). The shaded bands show the systematic uncertainty on the measurements (see Tables IV and V). A 5.8% uncertainty on the integrated luminosity is not included. The dashed lines indicate the PDF uncertainty on the theoretical predictions. For presentation, the measurements in different $|y^{jet}|$ regions are scaled by different global factors. Factors ($\times 10^6$), ($\times 10^3$), ($\times 10^{-3}$), and ($\times 10^{-6}$) are used in the regions $|y^{jet}| < 0.1$, $0.1 < |y^{jet}| < 0.7$, $1.1 < |y^{jet}| < 1.6$, and $1.6 < |y^{jet}| < 2.1$, respectively.

uncertainty on the measured cross sections at high p_T^{jet}, compared to that on the theoretical predictions, indicates that the data presented in this article will contribute to a better understanding of the gluon PDF.

Finally, in the region $0.1 < |y^{jet}| < 0.7$, the analysis is repeated using different values for D in the k_T algorithm: $D = 0.5$ and $D = 1.0$. In both cases, good agreement is observed between the measured cross sections and the NLO pQCD predictions in the whole range in p_T^{jet} (see Fig. 11 and Tables VI and VII). The corresponding χ^2 tests give probabilities of 84% and 22% for $D = 0.5$ and $D = 1.0$, respectively. As D decreases, the measurement is less sensitive to contributions from multiple $p\bar{p}$ interactions per bunch crossing, and the presence and proper modeling of the underlying event. For $D = 0.5$ ($D = 1.0$), the value for $\delta_{p_T}^{mi}$ becomes $1.18 \pm 0.12 (3.31 \pm 0.47)$ GeV/c, and the parton-to-hadron correction factor applied to the pQCD predictions is $C_{HAD} = 1.1$ ($C_{HAD} = 1.4$) at low p_T^{jet}.

XIII. SUMMARY AND CONCLUSIONS

We have presented results on inclusive jet production in $p\bar{p}$ collisions at $\sqrt{s} = 1.96$ TeV for jets with transverse momentum $p_T^{jet} > 54$ GeV/c and rapidity in the region $|y^{jet}| < 2.1$, using the k_T algorithm and based on 1.0 fb^{-1} of CDF run II data. The measured cross sections are in agreement with NLO pQCD predictions after the necessary nonperturbative parton-to-hadron corrections are taken into account. The results reported in this article should contribute to a better understanding of the gluon PDF inside the proton when used in QCD global fits.

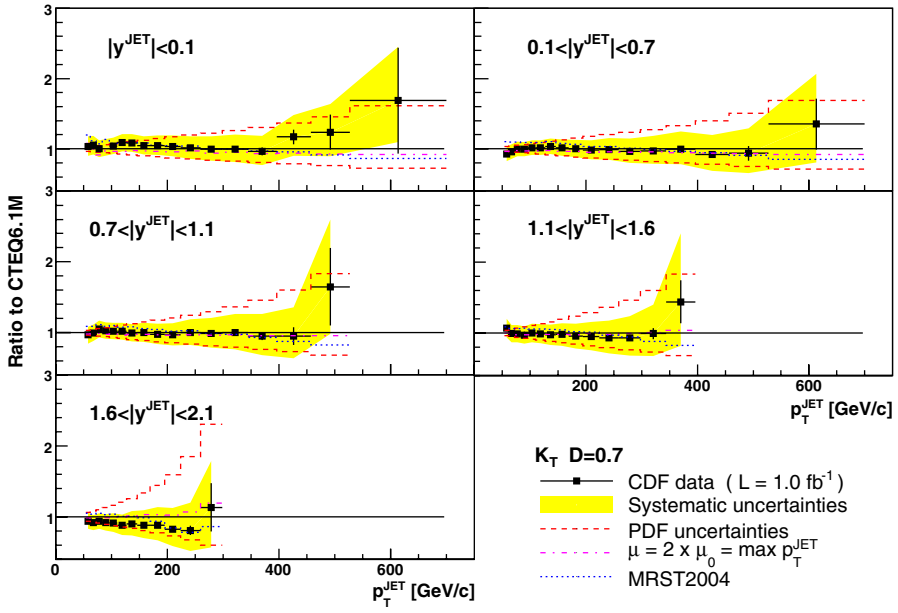

FIG. 10 (color online). Ratio data/theory as a function of p_T^{jet} in different $|y^{jet}|$ regions. The error bars (shaded bands) show the total statistical (systematic) uncertainty on the data. A 5.8% uncertainty on the integrated luminosity is not included. The dashed lines indicate the PDF uncertainty on the theoretical predictions. The dotted lines present the ratio of NLO pQCD predictions using MRST2004 and CTEQ6.1M PDFs. The dot-dashed lines show the ratios of pQCD predictions with $2\mu_0$ and μ_0.

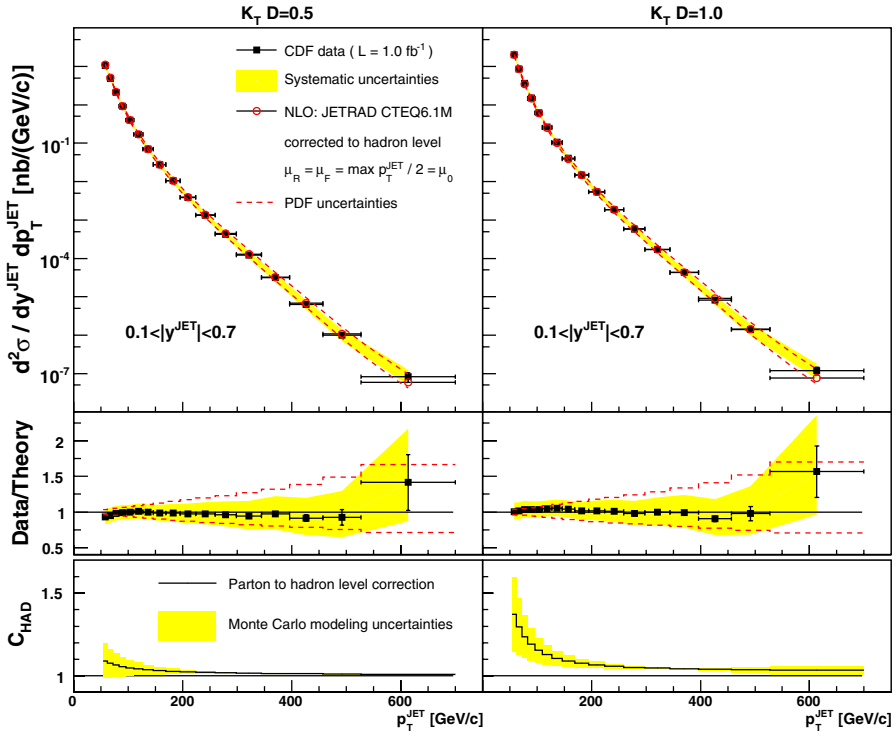

FIG. 11 (color online). (top) Measured inclusive differential jet cross sections (black squares) as a function of p_T^{jet} for jets with $p_T^{jet} > 54$ GeV/c and $0.1 < |y^{jet}| < 0.7$ using the k_T parameter $D = 0.5$ (left) and $D = 1.0$ (right), compared to NLO pQCD predictions (open circles). The shaded bands show the total systematic uncertainty on the measurements (see Tables VI and VII). A 5.8% uncertainty on the integrated luminosity is not included. The dashed lines indicate the PDF uncertainty on the theoretical predictions. (middle) Ratio data/theory as a function of p_T^{jet} for $D = 0.5$ (left) and $D = 1.0$ (right). (bottom) Magnitude of the parton-to-hadron corrections, $C_{HAD}(p_T^{jet})$, used to correct the NLO pQCD predictions for $D = 0.5$ (left) and $D = 1.0$ (right). The shaded bands indicate the quoted Monte Carlo modeling uncertainty.

ACKNOWLEDGMENTS

We thank the Fermilab staff and the technical staffs of the participating institutions for their vital contributions. This work was supported by the U.S. Department of Energy and National Science Foundation; the Italian Istituto Nazionale di Fisica Nucleare; the Ministry of Education, Culture, Sports, Science and Technology of Japan; the Natural Sciences and Engineering Research Council of Canada; the National Science Council of the Republic of China; the Swiss National Science Foundation; the A. P. Sloan Foundation; the Bundesministerium für Bildung und Forschung, Germany; the Korean Science and Engineering Foundation and the Korean Research Foundation; the Particle Physics and Astronomy Research Council and the Royal Society, UK; the Institut National de Physique Nucleaire et Physique des Particules/CNRS; the Russian Foundation for Basic Research; the Comisión Interministerial de Ciencia y Tecnología, Spain; the European Community's Human Potential Programme under Contract No. HPRN-CT-2002-00292; and the Academy of Finland.

APPENDIX A: CORRELATIONS OF SYSTEMATIC UNCERTAINTIES

The correlations among systematic uncertainties in different p_T^{jet} bins and $|y^{jet}|$ regions are studied in detail. The uncertainty on the absolute jet energy scale is decomposed into different sources considered independent but fully correlated across p_T^{jet} bins and $|y^{jet}|$ regions. A $\pm 1.8\%$ uncertainty on the absolute energy scale, independent of p_T^{jet}, results from the sum in quadrature of four different contributions [45]: a $\pm 0.5\%$ uncertainty from the calorimeter stability versus time, a $\pm 1.0\%$ uncertainty due to the modeling of the jet fragmentation, a $\pm 0.5\%$ uncertainty from the simulation of the electromagnetic calorimeter response, and a $\pm 1.3\%$ uncertainty from the simulation of the calorimeter response at the boundary between calorimeter towers. Other contributions to the absolute energy scale uncertainty come from the description of the calorimeter response to hadrons for different ranges in hadron momentum [45]. Table VIII shows the resulting relative contributions to the quoted systematic uncertainty on the measured cross sections related to the absolute jet energy scale uncertainty.

TABLE VI. Systematic uncertainties (in percent) on the measured inclusive jet differential cross section as a function of p_T^{jet}, for jets in the region $0.1 < |y^{jet}| < 0.7$ and using $D = 0.5$ and $D = 1.0$ (see Fig. 11). The different columns follow the discussion in Sec. X. An additional 5.8% uncertainty on the integrated luminosity is not included.

Systematic uncertainties [%] $(0.1 < \lvert y^{jet}\rvert < 0.7)$ $(D = 0.5)$					
p_T^{jet} [GeV/c]	Jet energy scale	Resolution	Unfolding	p_T^{jet}-spectra	$\delta_{p_T}^{mi}$
54–62	$^{+9.9}_{-9.2}$	$^{+2.4}_{-2.3}$	± 5.4	± 0.6	$^{+0.8}_{-0.8}$
62–72	$^{+9.8}_{-9.0}$	$^{+2.4}_{-2.2}$	± 4.8	± 0.6	$^{+0.7}_{-0.7}$
72–83	$^{+9.8}_{-8.9}$	$^{+2.3}_{-2.2}$	± 4.3	± 0.6	$^{+0.6}_{-0.7}$
83–96	$^{+9.7}_{-8.9}$	$^{+2.2}_{-2.1}$	± 3.8	± 0.6	$^{+0.6}_{-0.6}$
96–110	$^{+9.8}_{-9.0}$	$^{+2.2}_{-2.1}$	± 3.4	± 0.6	$^{+0.5}_{-0.5}$
110–127	$^{+10.0}_{-9.4}$	$^{+2.1}_{-2.0}$	± 3.1	± 0.6	$^{+0.5}_{-0.5}$
127–146	$^{+10.4}_{-9.9}$	$^{+2.1}_{-2.0}$	± 2.8	± 0.6	$^{+0.4}_{-0.4}$
146–169	$^{+11.2}_{-10.8}$	$^{+2.1}_{-2.0}$	± 2.5	± 0.5	$^{+0.4}_{-0.4}$
169–195	$^{+12.5}_{-11.9}$	$^{+2.1}_{-2.1}$	± 2.3	± 0.4	$^{+0.4}_{-0.4}$
195–224	$^{+14.3}_{-13.3}$	$^{+2.2}_{-2.2}$	± 2.1	± 0.3	$^{+0.4}_{-0.3}$
224–259	$^{+16.6}_{-15.0}$	$^{+2.4}_{-2.4}$	± 1.9	± 0.2	$^{+0.3}_{-0.3}$
259–298	$^{+19.3}_{-17.0}$	$^{+2.7}_{-2.7}$	± 1.8	± 0.1	$^{+0.3}_{-0.3}$
298–344	$^{+22.3}_{-19.4}$	$^{+3.1}_{-3.2}$	± 1.6	± 0.1	$^{+0.3}_{-0.3}$
344–396	$^{+25.7}_{-22.1}$	$^{+3.7}_{-3.8}$	± 1.5	± 0.2	$^{+0.3}_{-0.3}$
396–457	$^{+30.7}_{-25.5}$	$^{+4.5}_{-4.6}$	± 1.4	± 0.5	$^{+0.3}_{-0.3}$
457–527	$^{+39.5}_{-29.7}$	$^{+5.5}_{-5.6}$	± 1.3	± 1.3	$^{+0.3}_{-0.2}$
527–700	$^{+52.6}_{-37.7}$	$^{+7.4}_{-7.3}$	± 1.2	± 4.2	$^{+0.3}_{-0.2}$
Systematic uncertainties [%] $(0.1 < \lvert y^{jet}\rvert < 0.7)$ $(D = 1.0)$					
p_T^{jet} [GeV/c]	Jet energy scale	Resolution	Unfolding	p_T^{jet}-spectra	$\delta_{p_T}^{mi}$
54–62	$^{+10.7}_{-9.4}$	$^{+2.7}_{-2.7}$	± 5.6	± 0.4	$^{+3.5}_{-2.9}$
62–72	$^{+10.4}_{-9.3}$	$^{+2.6}_{-2.5}$	± 4.9	± 0.4	$^{+3.0}_{-2.6}$
72–83	$^{+10.3}_{-9.2}$	$^{+2.4}_{-2.4}$	± 4.2	± 0.4	$^{+2.6}_{-2.4}$
83–96	$^{+10.2}_{-9.2}$	$^{+2.3}_{-2.3}$	± 3.7	± 0.4	$^{+2.3}_{-2.2}$
96–110	$^{+10.2}_{-9.3}$	$^{+2.2}_{-2.2}$	± 3.2	± 0.4	$^{+2.1}_{-2.0}$
110–127	$^{+10.4}_{-9.6}$	$^{+2.1}_{-2.1}$	± 2.8	± 0.4	$^{+1.9}_{-1.8}$
127–146	$^{+10.8}_{-10.1}$	$^{+2.0}_{-2.0}$	± 2.5	± 0.4	$^{+1.7}_{-1.7}$
146–169	$^{+11.5}_{-10.8}$	$^{+1.9}_{-1.9}$	± 2.1	± 0.4	$^{+1.6}_{-1.6}$
169–195	$^{+12.6}_{-11.8}$	$^{+1.9}_{-2.0}$	± 1.9	± 0.4	$^{+1.5}_{-1.4}$
195–224	$^{+13.9}_{-13.1}$	$^{+1.9}_{-2.0}$	± 1.6	± 0.3	$^{+1.4}_{-1.3}$
224–259	$^{+15.8}_{-14.7}$	$^{+2.1}_{-2.2}$	± 1.4	± 0.3	$^{+1.3}_{-1.3}$
259–298	$^{+18.0}_{-16.6}$	$^{+2.4}_{-2.5}$	± 1.3	± 0.2	$^{+1.3}_{-1.2}$
298–344	$^{+20.8}_{-18.8}$	$^{+2.8}_{-2.9}$	± 1.1	± 0.2	$^{+1.2}_{-1.1}$
344–396	$^{+24.5}_{-21.4}$	$^{+3.4}_{-3.6}$	± 1.0	± 0.2	$^{+1.2}_{-1.1}$
396–457	$^{+30.1}_{-24.7}$	$^{+4.3}_{-4.4}$	± 0.8	± 0.5	$^{+1.1}_{-1.0}$
457–527	$^{+38.8}_{-29.5}$	$^{+5.4}_{-5.4}$	± 0.7	± 1.1	$^{+1.1}_{-1.0}$
527–700	$^{+49.8}_{-37.6}$	$^{+7.3}_{-7.2}$	± 0.6	± 3.4	$^{+1.0}_{-0.9}$

The rest of the systematic uncertainties on the measured cross sections, including that on the total integrated luminosity, are also assumed to be independent and fully correlated across p_T^{jet} bins and $|y^{jet}|$ regions, except those related to the β_{data}/β_{mc} ratio, for which uncertainties in different $|y^{jet}|$ regions are uncorrelated.

TABLE VII. Measured inclusive jet differential cross section as a function of p_T^{jet} for jets in the region $0.1 < |y^{jet}| < 0.7$ using $D = 0.5$ and $D = 1.0$ (see Fig. 11). An additional 5.8% uncertainty on the integrated luminosity is not included. The parton-to-hadron correction factors, $C_{HAD}(p_T^{jet})$, are applied to the pQCD predictions.

$\frac{d^2\sigma}{dp_T^{jet}dy^{jet}}$ $(0.1 < \lvert y^{jet}\rvert < 0.7)$ $(D = 0.5)$		
p_T^{jet} [GeV/c]	$\sigma \pm$ (stat) $\pm$ (sys) [nb/(GeV/c)]	C_{HAD} parton $\rightarrow$ hadron
54–62	$(10.5 \pm 0.2^{+1.2}_{-1.1}) \times 10^{0}$	1.089 ± 0.104
62–72	$(4.81 \pm 0.03^{+0.54}_{-0.50}) \times 10^{0}$	1.076 ± 0.086
72–83	$(2.09 \pm 0.01^{+0.23}_{-0.21}) \times 10^{0}$	1.064 ± 0.070
83–96	$(0.91 \pm 0.01^{+0.10}_{-0.09}) \times 10^{0}$	1.055 ± 0.057
96–110	$(3.95 \pm 0.04^{+0.42}_{-0.39}) \times 10^{-1}$	1.047 ± 0.047
110–127	$(1.71 \pm 0.02^{+0.18}_{-0.17}) \times 10^{-1}$	1.041 ± 0.037
127–146	$(0.71 \pm 0.01^{+0.08}_{-0.07}) \times 10^{-1}$	1.035 ± 0.029
146–169	$(2.76 \pm 0.02^{+0.32}_{-0.31}) \times 10^{-2}$	1.030 ± 0.023
169–195	$(1.04 \pm 0.01^{+0.14}_{-0.13}) \times 10^{-2}$	1.026 ± 0.017
195–224	$(3.87 \pm 0.02^{+0.57}_{-0.53}) \times 10^{-3}$	1.022 ± 0.012
224–259	$(1.34 \pm 0.01^{+0.23}_{-0.21}) \times 10^{-3}$	1.019 ± 0.008
259–298	$(4.26 \pm 0.04^{+0.83}_{-0.74}) \times 10^{-4}$	1.017 ± 0.005
298–344	$(1.22 \pm 0.02^{+0.28}_{-0.24}) \times 10^{-4}$	1.015 ± 0.002
344–396	$(3.16 \pm 0.09^{+0.82}_{-0.71}) \times 10^{-5}$	1.013 ± 0.001
396–457	$(6.30 \pm 0.32^{+1.96}_{-1.63}) \times 10^{-6}$	1.011 ± 0.002
457–527	$(1.01 \pm 0.12^{+0.40}_{-0.31}) \times 10^{-6}$	1.010 ± 0.003
527–700	$(0.83 \pm 0.23^{+0.44}_{-0.32}) \times 10^{-7}$	1.008 ± 0.005
$\frac{d^2\sigma}{dp_T^{jet}dy^{jet}}$ $(0.1 < \lvert y^{jet}\rvert < 0.7)$ $(D = 1.0)$		
p_T^{jet} [GeV/c]	$\sigma \pm$ (stat) $\pm$ (sys) [nb/(GeV/c)]	C_{HAD} parton $\rightarrow$ hadron
54–62	$(20.0 \pm 0.2^{+2.6}_{-2.3}) \times 10^{0}$	1.372 ± 0.227
62–72	$(8.65 \pm 0.04^{+1.1}_{-1.0}) \times 10^{0}$	1.296 ± 0.171
72–83	$(3.59 \pm 0.02^{+0.42}_{-0.39}) \times 10^{0}$	1.236 ± 0.129
83–96	$(1.49 \pm 0.01^{+0.17}_{-0.16}) \times 10^{0}$	1.190 ± 0.098
96–110	$(6.27 \pm 0.05^{+0.70}_{-0.65}) \times 10^{-1}$	1.155 ± 0.075
110–127	$(2.63 \pm 0.03^{+0.29}_{-0.27}) \times 10^{-1}$	1.127 ± 0.057
127–146	$(1.05 \pm 0.01^{+0.12}_{-0.11}) \times 10^{-1}$	1.105 ± 0.044
146–169	$(4.04 \pm 0.03^{+0.48}_{-0.45}) \times 10^{-2}$	1.088 ± 0.034
169–195	$(1.48 \pm 0.01^{+0.19}_{-0.18}) \times 10^{-2}$	1.075 ± 0.026
195–224	$(5.41 \pm 0.02^{+0.77}_{-0.73}) \times 10^{-3}$	1.065 ± 0.019
224–259	$(1.86 \pm 0.01^{+0.30}_{-0.28}) \times 10^{-3}$	1.057 ± 0.013
259–298	$(5.77 \pm 0.04^{+1.05}_{-1.00}) \times 10^{-4}$	1.050 ± 0.008
298–344	$(1.70 \pm 0.02^{+0.36}_{-0.32}) \times 10^{-4}$	1.045 ± 0.003
344–396	$(4.26 \pm 0.10^{+1.05}_{-0.93}) \times 10^{-5}$	1.041 ± 0.003
396–457	$(8.17 \pm 0.36^{+2.49}_{-2.06}) \times 10^{-6}$	1.038 ± 0.009
457–527	$(1.39 \pm 0.14^{+0.55}_{-0.42}) \times 10^{-6}$	1.036 ± 0.015
527–700	$(1.19 \pm 0.27^{+0.60}_{-0.46}) \times 10^{-7}$	1.033 ± 0.027

A global χ^2 test is performed according to the formula

$$\chi^2 = \sum_{j=1}^{76} \frac{[\sigma_j^d - \sigma_j^{th}(\bar{s})]^2}{[\delta\sigma_j^d]^2 + [\delta\sigma_j^{th}(\bar{s})]^2} + \sum_{i=1}^{17} [s_i]^2, \qquad \text{(A1)}$$

where σ_j^d is the measured cross section for data point j,

TABLE VIII. Relative contributions (in percent) to the quoted systematic uncertainty on the measured cross sections related to the absolute jet energy scale uncertainty. The second column corresponds to a $\pm 1.8\%$ uncertainty on the absolute energy scale, as discussed in the text. Sources are considered independent and fully correlated in $p_{\mathrm{T}}^{\mathrm{jet}}$ and $|y^{\mathrm{jet}}|$.

$p_{\mathrm{T}}^{\mathrm{jet}}$ [GeV/c]	$p_{\mathrm{T}}^{\mathrm{jet}}$ independent uncertainty	Response to hadrons $p < 12$ GeV/c	$12 < p < 20$ GeV/c	$p > 20$ GeV/c
54–62	90.3	37.8	15.2	13.5
62–72	90.2	35.2	16.1	19.1
72–83	89.9	31.9	17.0	24.6
83–96	89.2	28.8	17.3	30.1
96–110	88.0	26.0	16.9	35.8
110–127	86.4	22.7	16.4	41.9
127–146	84.3	20.0	15.1	47.7
146–169	82.1	17.2	14.1	52.6
169–195	79.8	14.6	12.7	57.0
195–224	77.6	12.5	11.5	60.7
224–259	75.7	10.7	10.3	63.6
259–298	73.8	9.1	9.2	66.2
298–344	72.1	7.8	8.2	68.3
344–396	70.5	6.8	7.3	70.2
396–457	69.2	5.8	6.4	71.7
457–527	68.0	5.0	5.7	72.9
527–700	66.8	4.2	5.0	74.2

$\sigma_j^{\mathrm{th}}(\bar{s})$ is the corresponding prediction, and $\bar{s}$ denotes the vector of standard deviations, s_i, for the different independent sources of systematic uncertainty. The values for $\sigma_j^{\mathrm{th}}(\bar{s})$ are obtained from the nominal NLO pQCD prediction, where $\bar{s}$ includes the uncertainty on $\mathrm{C_{HAD}}$ but does not consider PDF uncertainties. The uncertainty on $\mathrm{C_{HAD}}$ is assumed to be fully correlated across $p_{\mathrm{T}}^{\mathrm{jet}}$ bins and $|y^{\mathrm{jet}}|$ regions. The sums in Eq. (A1) run over 76 data points and 17 independent sources of systematic uncertainty, and the χ^2 is minimized with respect to $\bar{s}$. Correlations among systematic uncertainties are taken into account in $\sigma_j^{\mathrm{th}}(\bar{s})$. As an example, for a given source i, variations of s_i will coherently affect all the $\sigma_j^{\mathrm{th}}(\bar{s})$ values if the corresponding systematic uncertainties are considered fully correlated across $p_{\mathrm{T}}^{\mathrm{jet}}$ bins and $|y^{\mathrm{jet}}|$ regions.

[1] D. J. Gross and F. Wilczek, Phys. Rev. D **8**, 3633 (1973); H. Fritzsch, M. Gell-Mann, and H. Leutwyler, Phys. Lett. **47B**, 365 (1973).

[2] The run II at the Tevatron started in 2002 colliding proton and antiproton beams with a center-of-mass energy of 1.96 TeV. During the run I, that ended in 1996, the center-of-mass energy was set to 1.8 TeV.

[3] A. Abulencia *et al.* (CDF Collaboration), Phys. Rev. Lett. **96**, 122001 (2006).

[4] A. Abulencia *et al.* (CDF Collaboration), Phys. Rev. D **74**, 071103(R) (2006).

[5] T. Affolder *et al.* (CDF Collaboration), Phys. Rev. D **64**, 032001 (2001); **65**, 039903(E) (2002).

[6] B. Abbott *et al.* (D0 Collaboration), Phys. Rev. Lett. **82**, 2451 (1999).

[7] V. M. Abazov *et al.* (D0 Collaboration), Phys. Lett. B **525**, 211 (2002).

[8] S. Catani *et al.*, Nucl. Phys. **B406**, 187 (1993).

[9] S. D. Ellis and D. E. Soper, Phys. Rev. D **48**, 3160 (1993).

[10] We use a cylindrical coordinate system about the beam axis in which the proton defines the positive z-direction, θ is the polar angle, and ϕ is the azimuthal angle. We define $E_{\mathrm{T}} = E\sin\theta$, $p_{\mathrm{T}} = p\sin\theta$, $\eta = -\ln(\tan(\frac{\theta}{2}))$, and $y = \frac{1}{2} \times \ln(\frac{E+p_z}{E-p_z})$.

[11] W. T. Giele, E. W. N. Glover, and D. A. Kosower, Nucl. Phys. **B403**, 633 (1993).

[12] J. Pumplin *et al.*, J. High Energy Phys. 07 (2002) 012.

[13] A. D. Martin *et al.*, Eur. Phys. J. C **23**, 73 (2002).

[14] The hadron level in the Monte Carlo generators is defined using all final-state particles with lifetime above 10^{-11} s.

[15] D. Acosta *et al.* (CDF Collaboration), Phys. Rev. D **71**, 032001 (2005).

[16] A. Sill *et al.*, Nucl. Instrum. Methods Phys. Res., Sect. A **447**, 1 (2000); A. Affolder *et al.*, Nucl. Instrum. Methods Phys. Res., Sect. A **453**, 84 (2000); C. S. Hill, Nucl. Instrum. Methods Phys. Res., Sect. A **530**, 1 (2004).

[17] T. Affolder *et al.*, Nucl. Instrum. Methods Phys. Res., Sect. A **526**, 249 (2004).

[18] L. Balka *et al.*, Nucl. Instrum. Methods Phys. Res., Sect. A **267**, 272 (1988); S. R. Hahn *et al.*, Nucl. Instrum. Methods Phys. Res., Sect. A **267**, 351 (1988).

[19] S. Bertolucci *et al.*, Nucl. Instrum. Methods Phys. Res., Sect. A **267**, 301 (1988).

[20] R. Oishi, Nucl. Instrum. Methods Phys. Res., Sect. A **453**, 227 (2000); M. G. Albrow *et al.*, Nucl. Instrum. Methods Phys. Res., Sect. A **480**, 524 (2002).

[21] D. Acosta *et al.*, Nucl. Instrum. Methods Phys. Res., Sect. A **494**, 57 (2002).

[22] The four-momentum of a calorimeter section is computed using its energy and the unit vector joining the primary interaction vertex in the event and the center of calorimeter section, where the latter is defined in terms of the position of its typical shower maximum.

[23] B. L. Winer, Int. J. Mod. Phys. A **16S1C**, 1169 (2001).

[24] In order to reduce online trigger rates, different prescale factors are applied to trigger paths. For a given trigger path, a prescale of 1000 would indicate that only one of every 1000 events satisfying the trigger requirements is selected.

[25] A trigger tower is constructed using *a priori* defined pairs of adjacent calorimeter towers.

[26] F. Abe *et al.* (CDF Collaboration), Phys. Rev. D **45**, 1448 (1992).

[27] A. Abulencia *et al.* (CDF Collaboration), FERMILAB Report No. FERMILAB-PUB-05-360-E.

[28] $\not\!\!E_{\mathrm{T}}$ is defined as the norm of $-\sum_i E_{\mathrm{T}}^i \cdot \vec{n}_i$, where $\vec{n}_i$ is the unit vector in the azimuthal plane that points from the beam line to the ith calorimeter tower.

[29] R. Brun *et al.*, Technical Report CERN-DD/EE/84-1, 1987 (unpublished).

[30] G. Grindhammer, M. Rudowicz, and S. Peters, Nucl. Instrum. Methods Phys. Res., Sect. A **290**, 469 (1990).

[31] T. Sjöstrand *et al.*, Comput. Phys. Commun. **135**, 238 (2001).

[32] G. Corcella *et al.*, J. High Energy Phys. 01 (2001) 010.

[33] H. L. Lai *et al.*, Eur. Phys. J. C **12**, 375 (2000).

[34] PYTHIA-TUNE A Monte Carlo samples are generated using the following tuned parameters in PYTHIA: PARP(67) = 4.0, MSTP(82) = 4, PARP(82) = 2.0, PARP(84) = 0.4, PARP(85) = 0.9, PARP(86) = 0.95, PARP(89) = 1800.0, and PARP(90) = 0.25.

[35] T. Affolder *et al.* (CDF Collaboration), Phys. Rev. D **65**, 092002 (2002).

[36] D. Acosta *et al.* (CDF Collaboration), Phys. Rev. D **71**, 112002 (2005).

[37] B. Andersson *et al.*, Phys. Rep. **97**, 31 (1983).

[38] T. Sjöstrand, Comput. Phys. Commun. **39**, 347 (1986).

[39] B. R. Webber, Nucl. Phys. **B238**, 492 (1984).

[40] P. Bagnaia *et al.* (UA2 Collaboration), Phys. Lett. **144B**, 283 (1984).

[41] The different behavior of $\sigma^{\mathrm{data}}_{p_{\mathrm{T}}^{\mathrm{jet}}}/\sigma^{\mathrm{mc}}_{p_{\mathrm{T}}^{\mathrm{jet}}}$ observed as a function of $|y^{\mathrm{jet}}_{\mathrm{cal}}|$ can be understood in terms of the calorimeter layout, the presence of gaps between calorimeter systems, and a different level of accuracy in the simulation of the calorimeter response to jets as a function of rapidity.

[42] If considered event-by-event, β is equivalent to $p_{\mathrm{T,cal}}^{\mathrm{test\ jet}}/p_{\mathrm{T,cal}}^{\mathrm{ref\ jet}}$. However, Eq. (2) is preferred since Δ follows a Gaussian distribution while the ratio $p_{\mathrm{T,cal}}^{\mathrm{test\ jet}}/p_{\mathrm{T,cal}}^{\mathrm{ref\ jet}}$ suffers from important non-Gaussian tails.

[43] $\hat{p}_t$ is defined for two-body reactions in terms of Mandelstam variables as $\hat{p}_t = \sqrt{\frac{\hat{t}\cdot\hat{u}}{\hat{s}}}$.

[44] O. Norniella, Ph.D. thesis, Universidad Autónoma de Barcelona, 2007.

[45] A. Bhatti *et al.*, Nucl. Instrum. Methods Phys. Res., Sect. A **566**, 375 (2006).

[46] J. Pumplin *et al.*, Phys. Rev. D **65**, 014013 (2001).